ISTANBUL TECHNICAL UNIVERSITY ★ GRADUATE SCHOOL

MEASUREMENT BASED AIR TO AIR AND AIR TO GROUND DRONE COMMUNICATION CHANNEL MODELING

M.Sc. THESIS

Burak EDE

Department of Electronics and Communication Engineering

Telecommunication Engineering Programme

MAY 2023

ISTANBUL TECHNICAL UNIVERSITY ★ GRADUATE SCHOOL

MEASUREMENT BASED AIR TO AIR AND AIR TO GROUND DRONE COMMUNICATION CHANNEL MODELING

M.Sc. THESIS

Burak EDE
(504191305)

Department of Electronics and Communication Engineering

Telecommunication Engineering Programme

Thesis Advisor: Prof. Dr. Hakan Ali ÇIRPAN

MAY 2023

İSTANBUL TEKNİK ÜNİVERSİTESİ ★ LİSANSÜSTÜ EĞİTİM ENSTİTÜSÜ

ÖLÇÜM TABANLI HAVADAN HAVAYA VE HAVADAN YERE DRONE İLETİŞİM KANALI MODELLEME

YüKSEK LİSANS TEZİ

Burak EDE
(504191305)

Elektronik ve Haberleşme Mühendisliği Anabilim Dalı

Telekomünikasyon Mühendisliği Programı

Tez Danışmanı: Prof. Dr. Hakan Ali ÇIRPAN

MAYIS 2023

Burak EDE, a M.Sc. student of ITU Graduate School student ID 504191305, successfully defended the thesis entitled “MEASUREMENT BASED AIR TO AIR AND AIR TO GROUND DRONE COMMUNICATION CHANNEL MODELING”, which he/she prepared after fulfilling the requirements specified in the associated legislations, before the jury whose signatures are below.

Thesis Advisor : **Prof. Dr. Hakan Ali ÇIRPAN** ....
Istanbul Technical University

Jury Members : **Prof. Dr. Selçuk PAKER** ....
Istanbul Technical University

Dr. İbrahim HÖKELEK ....
TÜBİTAK BİLGEM

Date of Submission : 11 April 2023
Date of Defense : 05 May 2023

To my family,

FOREWORD

First of all, I would like to express my thanks to my advisor, Prof. Dr. Hakan Ali Çırpan, who has never given up his support in making this study.

At the same time, I would like to thank especially Dr. Ali Rıza Ekti and also Prof. Dr. Serhan Yarkan and Assoc. Dr. Tunçer Baykaş for their valuable contributions, who supported me a lot during this process.

In addition, I would like to thank TÜBİTAK BİLGEM HİSAR laboratory and my valuable colleagues for their support both in the measurement processes and mentally in this thesis.

Finally, I can’t thank my wife enough for giving meaning to my life and always supporting me.

May 2023

Burak EDE
(Electronics and Communication Engineer)

TABLE OF CONTENTS

Page

ABBREVIATIONS

4G : 4th–Generation
5G : 5th–Generation
6G : 6th–Generation
AP : Access point
A2A : Air–to–Air
A2G : Air–to–Ground
AWGN : Additive White Gaussian Noise
BW : Bandwidth
BB : Baseband
BS : Base station
CIR : Channel impulse response
CP : Circularly polarized
CW : Continuous wave
D2D : Device–to–device
dB : decibel
dBi : decibel isotropic
dBm : decibel over a milliwatt
DFT : Discrete Fourier transform
FFT : Fast Fourier Transform
FPGA : Field-programmable gate array
Gbps : Gigabit per second
GBSM : Geometry-based stochastic model
GHz : Gigahertz
GPS : Global positioning system
Hz : Hertz
I/Q : In–phase/quadrature
IF : Intermediate frequency
IoT : Internet of Things
IFFT : Inverse fast Fourier Transform
LOS : Line–of–sight
LNA : Low noise amplifier
LO : Local oscillator
LOL : Local oscillator leak
M2M : Machine–to–machine
MHz : Megahertz
MLE : Maximum likelihood estimation
MIMO : Multiple–input multiple–output
MPC : Multipath component
NBSG : Narrow band signal generator
NGWN : Next generation wireless network

NLOS	: Nonline–of–sight
ppm	: Parts per million
PLE	: Path loss exponent
PDP	: Power delay profile
PPS	: Pulse per second
QoS	: Quality of service
RF	: Radio frequency
RSSI	: Received signal strength indicator
SDR	: Software defined radio
STFT	: Short time Fourier transform
SAGE	: Space-alternating generalized expectation-maximization
UHF	: Ultra high frequency
UAV	: Unmanned aerial vehicle
UDP	: User datagram protocol
USRP	: Universal Software Based Hardware
VNA	: Vector network analyzer

SYMBOLS

$\boldsymbol{\eta}$: Path loss exponent
$\boldsymbol{d}$: Transmitter–receiver separation
$\boldsymbol{d_0}$: Reference distance
$\boldsymbol{PL_0}$: Free–space intercept
$\boldsymbol{\mu_{\mathrm{LOS}}}$: Large–scale characteristic losses for line–of–sight (LOS)
$\boldsymbol{\omega}$: Baseband frequency of the tone signal
$\boldsymbol{\psi}$: Phase error due to Q component
$\boldsymbol{\beta_{\mathrm{I}}}$,$\boldsymbol{\beta_{\mathrm{Q}}}$: Direct current (DC) component for each path
$\boldsymbol{\alpha}$: Amplitude error caused by the I component

LIST OF TABLES

LIST OF FIGURES

MEASUREMENT BASED
AIR TO AIR AND AIR TO GROUND
DRONE COMMUNICATION CHANNEL MODELING

SUMMARY

Unmanned aerial vehicle (UAV) has become widespread and has brought various communication problems. Especially the wireless communication area receiver and transmitter design is of great importance for UAV–Ground and UAV–UAV scenarios. Furthermore, powered by the advances in microelectronics technologies, UAVs provide a vast variety of services ranging from surveillance to delivery in both military and civilian domains. It is clear that a successful operation in those services relies heavily on wireless communication technologies. Even though wireless communication techniques could be considered to reach a certain level of maturity, wireless communication links including UAVs should be regarded in a different way due to the peculiar characteristics of UAVs such as agility in 3D spatial domain and versatility in modes of operation. Such mobility characteristics in a vast variety of environmental diversity render links including UAV different from those in traditional, terrestrial mobility scenarios. Furthermore, UAVs are critical instruments for network operators in order to provide basic voice and short messaging services for narrow band communication in and around disaster areas. It is obvious that such widespread use of UAVs under different scenarios and environments requires a better understanding the behavior of the communication links that include UAVs. In addition to, drones are emerging as a rapid solution to enable or support communication services in various scenarios such as sports events, natural disasters, macro base station malfunctions. Any operation scenario for drones requires a reliable, secure, and resilient wireless link to guarantee capacity and performance for users, which can only be achieved by obtaining detailed knowledge about the propagation channel.

Therefore, in Chapter 3, different measurement systems have been tried to be created for UAV channel modeling, but it has become difficult to obtain measurement based results due to physical problems arising from UAV and design of mobile measurement system. In addition, channel measurement systems with Universal Software Based Hardware (USRP), one of the software based radio devices and challenges will be mentioned.

In Chapter 4, details of a measurement campaign designed to collect data for large-scale propagation characterization of air–to–ground links operated by UAV at 446MHz are given. Data collection, post-processing, and measurement results are provided.

Chapter 5 investigates the large-scale channel propagation statistics for the LOS A2A drone communications. We conducted a measurement campaign at 5.8 GHz, using software defined radio based channel sounders and commercially available drones. To determine the path loss exponent, frequency-based, time-based and time–frequency

based methods are utilized. Accuracy of the proposed method is verified under ideal conditions in a well-isolated anechoic chamber before the actual measurement campaign to verify the performance in a free space path loss environment. The path loss exponent for A2A wireless drone channel is estimated with these verified methods.

ÖLÇÜM TABANLI
HAVADAN HAVAYA VE HAVADAN YERE
DRONE İLETİŞİM KANALI MODELLEME

ÖZET

İHA'ların savunma sanayisinden turizme kadar geniş bir yelpazede kullanılmaya başlandığı günümüzde, İHA'lar arasında haberleşme ihtiyacı büyük önem taşımaktadır. Buna göre kablosuz haberleşme tekniklerinin de kendisini buna adapte etmesi beklenmektedir. Kablosuz haberleşme teknolojileri açısından İHA'ların yaygınlaşması ve birçok yönden daha iyi çözümler sunması, haberleşme alanında çalışmayı zorunlu kılmıştır. Bu nedenle İHA'lar için bu anlamda yapılan çalışmalar son yıllarda hızla artmaktadır. Özellikle 4G ve 5G teknolojilerinde ve temelleri atılmaya devam edilen 6G teknolojilerinde, İHA haberleşmesine uygun bir alıcı ve verici tasarlamak için İHA kanal modellerinin oluşturulması gerekmektedir. Bu bağlamda kablosuz haberleşme alıcı ve verici tasarımı İHA-Yer ve İHA–İHA senaryoları için büyük önem taşımaktadır.

Ayrıca, mikro elektronik teknolojilerindeki gelişmelerden güç alan İHA, hem askeri hem de sivil alanlarda gözetimden teslimata kadar çok çeşitli hizmetler sunmaktadır. Bu hizmetlerde başarılı bir operasyonun büyük ölçüde kablosuz haberleşme teknolojilerine dayandığı açıktır. Kablosuz haberleşme tekniklerinin belirli bir olgunluk düzeyine ulaştığı düşünülebilse de, İHA'nın 3 boyutlu uzaysal alanda çeviklik ve çalışma modlarında çok yönlülük gibi kendine özgü özelliklerinden dolayı, İHA'yı içeren kablosuz haberleşme bağlantılarına farklı bir açıdan bakılmalıdır. Çok farklı çevresel koşullarındaki bu tür hareketlilik özellikleri, geleneksel, karasal hareketlilik senaryolarındakilerden (Mesela İHA'lar için) farklı haberleşme bağlantıları oluşturmaktadır. Ayrıca İHA, afet bölgelerinde ve çevresinde dar bant haberleşme için temel ses ve kısa mesajlaşma hizmetleri sağlamak amacıyla şebeke operatörleri için kritik araçlardır. İHA'nın farklı senaryo ve ortamlarda bu kadar yaygın bir şekilde kullanılmasının, İHA'yı içeren haberleşme bağlantılarının davranışının daha iyi anlaşılmasını gerektirdiği açıktır. Bahsedilen kullanım sorununun üstesinden gelmek için geleneksel strateji, kaynakların mümkün olduğunca sık yeniden kullanılmasıdır. Hücre bölme, anten bölümleme ve küçük hücre kavramları, mevcut bant genişliğinin etkin kullanımı yoluyla kapasiteyi artırmanın, iletim gücünü ve gürültünün etkisini azaltmanın öne çıkan örnekleridir. Piyasada küçük hücreli (mikro hücre, piko hücre, metro femtohücreleri anlamında femtocell, genel erişim femtohücreleri, kurumsal femtohücreler ve sınıf 3 seviye femtohücreler, vb.) çözümleri ile ilgili olarak, çoğunlukla sabit dağıtıma dayanan ürünler bulunmaktadır. Ancak İHA'ların ortaya çıkmasıyla birlikte kablosuz haberleşme topluluklarında birçok yönden bir paradigma kayması yaşanmıştır. 3B uzaysal alandaki çevikliği ve çalışma modlarındaki çok yönlülüğü göz önüne alındığında, İHA'lar çağdaş kablosuz mobil radyo haberleşme sistemlerinde neredeyse tamamen yeni bir bakış açısı getirmektedir. Acil durum

iletişiminden yönlendirme ve aktarmaya kadar uzanan İHA'lar, çeşitli kablosuz haberleşme senaryolarında umut verici çözüm adayları olarak kabul edilmektedir. Ek olarak, ortaya çıkan IoT kavramı, kablosuz radyo kapsamını çeşitli (ve nispeten zorlu yayılma) ortamlarına genişletmeyi zorunlu kılmaktadır. Çok çeşitli yayılma ortamlarının varlığında, başarılı bir kablosuz haberleşme bağlantısı, genişletilmiş ölçümlere ve karşılık gelen tasarımlara dayanan alıcı-vericilere bağlıdır.

Bunun yanı sıra spor karşılaşmaları, doğal afetler, makro baz istasyonu arızaları gibi çeşitli senaryolarda haberleşme hizmetlerini etkinleştirmek veya desteklemek için hızlı bir çözüm olarak İHA'lar ortaya çıkmaktadır. İHA'lar için herhangi bir operasyon senaryosu, kullanıcılar için kapasite ve performansı garanti etmek için güvenilir, güvenli ve esnek bir kablosuz bağlantı gerektirir; bu ise, yalnızca yayılma kanalı hakkında ayrıntılı bilgi edinerek elde edilebilmektedir.

Bu nedenle Bölüm 3'de İHA kanal modellemesi için oluşturulan ölçüm sisteminde kullanılan USRP'den mobil alıcı-verici tasarımına; kullanılan yükselticiden Raspberry Pi'ye; GPS modülünden uzaktan ölçüm alma yazılımına kadar birçok alanda sorunlar gözlenmekte ve buna uygun çözümler önerilmeye çalışılmaktadır. USRP'lerde merkez frekans kayması, DC kaçağı, I/Q dengesizliği gözlenmiş buna çözüm olarak sırasıyla frekans kayması kestiriminden sonra alıcıda frekans kayması düzeltilmesi, DC sızıntısına özgü süzgeçlerin tasarlanması, I/Q dengesizliğinde matrise dayalı dengesizlik kestirimi ve düzeltilmesi veya ikinci derece I/Q istatistiklerine bakarak düzeltme gibi çözümler önerilmektedir. Ayrıca mobil ölçüm sistemi oluşturmada kullanılan yükselticilerde dikkat edilmesi gereken hususlar, bunlara uygun DC-DC çevirici ile güç kaynağı seçimi, uzaktan kontrol etmek için Raspberry Pi 4B nasıl kullanıldığına ve alıcı ve vericinin konumunu takip etmek için GPS modülünün nasıl kullanıldığına da yer verilmektedir. Ayrıca bahsedilen cihazların birbiriyle nasıl haberleşeceği, kanal modeli için hangi yöntemin kullanılacağı, uzaktan nasıl bağlanılacağı ve ölçümün parametrik olarak nasıl kontrol edileceğine dair ifadelere yer verilmektedir. İHA kanal modellemesi yapılabilmesi için farklı ölçüm sistemleri oluşturulmaya çalışılmış, ancak İHA'dan kaynaklanan fiziksel problemler ve mobil ölçüm sisteminin tasarımı nedeniyle ölçüm tabanlı sonuçların elde edilmesi zorlaşmıştır. Ayrıca yazılım tabanlı telsiz cihazlarından USRP ile kanal ölçüm sistemlerinden ve zorluklarından bahsedilmektedir.

Bölüm 4'te, dar bant varsayımı altında 446 MHz'de İHA tarafından işletilen havadan yere bağlantıların büyük ölçekli yayılma karakterizasyonu için veri toplamak üzere tasarlanmış bir ölçüm sisteminin detayları verilmektedir. Veri toplama, son işleme ve ölçüm sonuçları sağlanır. UHF bandının yeniden düzenlenmesinin acil durum durumları için yeni fırsatlar sunacağı gerçeğinden dolayı, 446MHz'de İHA havadan karaya kanallar için bir ölçüm sisteminin sonuçları sunulmaktadır. Ölçüm verilerine dayanarak, çevre ile birlikte yüksekliğin dikkate alınması gereken önemli bir faktör olduğu gösterilmiştir. Bu nedenle, gelecekteki çalışmalarda, farklı konum ve topografyalardaki çevre etkisini de dahil ederek sonuçlarımızı çoklu frekans aralıklarına genişletilmesi düşünülmektedir.

Bölüm 5, büyük ölçekli görüş hattı yol kaybı bileşenlerinin katı bir ölçüme dayalı modellemesini sunarak, İHA'lar arasındaki havadan havaya (H–H) kablosuz haberleşme kanallarının özelliklerinin daha iyi anlaşılması için yapılan çalışma sunulmaktadır. Bu bölüm, böyle bir amaç için sağlam bir ölçüm düzeni geliştirmenin zorlukları hakkında bir fikir vermekte, ancak daha da önemlisi, yürütülen kapsamlı ölçüm sistemi, kırsal alanlarda 5.8GHz'de iletişim kuran alçak irtifa İHA'lar için büyük ölçekli bir H–H görüş hattı yol kaybı modeli sunmaktadır. Doğrulama ve istatistiksel modelleme amaçlarıyla hem yankısız oda hem de dış ortamda ölçümler yapılarak, İHA'ların ve H–H kanallarının kendine özgü özelliklerinin, boş alan yolu kaybından daha az bir yol kaybı üsseli ile sonuçlandığı gösterilmiştir. Araştırılan kanal dinleme yöntemi, diğer kanal dinleme yaklaşımlarına kıyasla nispeten çok düşük maliyetli olmasına rağmen önemli kanal bilgisi sağladığı için ilerlemeye değer görülmektedir. Önerilen kanal dinleme sistemi, gelecekteki çalışmalarda daha ileri analizler için bir temel sağlamaktadır, mesela daha geniş bantlar için kanal darbe yanıtının tahmini ve daha yüksek mertebeden kanal istatistikleri (örneğin, aşırı gecikme yayılımı, Doppler spektrumu) araştırma imkanı olabilecektir. Ayrıca, gölgeleme ve diğer sönümleme özelliklerini modellemek için NLOS senaryoları da kurulabilecektir. Tanıtılan ölçüm yöntemi, İHA uçuş süresini, frekans alanı tahminini ve kablosuz kapsama analizini optimize etmek için de kullanılabilir. Ayrıca, bu sistem, İHA gövde hareketinin ve İHA gövde kaymasının kablosuz sinyal alımı üzerindeki etkisini anlamak için kullanılabilir. Buna ilave olarak, İHA'ların hızla hareket ettiği yayılma ortamını tahmin etmek için ölçüm prosedürleri geliştirilebilir, mesela hızlı kanal karakterizasyonu gerektiren durumlarda kullanılabilir.

1. INTRODUCTION

Ubiquitous access has become an essential part of modern daily life. Services, applications, devices, and even products are equipped with wireless communication interfaces in such a way that diverse fields and domains are connected anywhere, anytime. In parallel with the escalating demand for high data rates, everywhere connectivity with mobility support becomes an indispensable design requirement for both contemporary and emerging wireless technologies. Although, it is expected that these wireless technologies should support crystal clear audio for voice, high–definition video downstreaming, very–low latency and 4K online gaming, low-power consumption transmission, and so on, it is more important to provide service on mission critical scenarios. Obviously, such an aggressive set of requirements comes at the expense of several conflicting list of parameters. Furthermore, realization of these requirements necessitate utilization of crucial resources such as bandwidth and power.

UAVs also known as drones are expected to cause a paradigm shift in wireless communications due to their peculiar characteristics such as agility in 3D spatial domain and versatility in modes of operation to act as flying base stations and relay nodes. Such versatility could be facilitated in various ways. Some of the prominent examples of possible use of drones include load balancing of wireless traffic in overpopulated zones and providing service in emergencies [1]. On the other hand, dynamic mobility patterns of drones pose serious concerns in modeling the overall performance of the wireless networks, which employ drones. It is clear that performance of such dynamic networks depends heavily on the statistical characteristics of the propagation channels among different wireless network elements. Since the propagation channels for fixed networks are well studied, main focus of Chapter 5 work is drone channels.

UAV channel models can coarsely be categorized in two classes: air–to–ground (A2G) and A2A channel models [2]. Each category can further be elaborated based on several other criteria such as dependence on measurement– or simulation–based data used or deterministic/stochastic models employed. A comprehensive model should be based on real–world measurement data and fortified with appropriate simulation models. Studies on UAV – ground channel modeling are given in [3–6]. In [3], channel characteristics are given for long distance air ground connections, depending on the measurements taken at 915 MHz. Compact receiver and transmitter structure is used in the measurement setup. There is an field-programmable gate array (FPGA) and frequency synthesizer in the structure. In [4], the channel properties of the UAV–to–ground connections on multi–path urban environments are examined. The channel model was obtained as a result of simulations using the ray tracing technique. In [5], channel parameters and channel impulse response at 850 MHz center frequency were obtained by using Space-alternating generalized expectation-maximization (SAGE) [7], which is a high resolution spectrum estimation algorithm. On the UAV side, a global positioning system (GPS)–disciplined oscillator capable of delivering 10MHz and 1 pulse per second (PPS) is connected to the USRP. In addition, a mini–computer was used to control the USRP and save data. On the ground station side, there is a USRP, a GPS disciplined oscillator, a power amplifier and a half–directional packaged vertical cone antenna. Finally, in [6], path loss properties for the air–to–ground radio channel are extracted using data generated by deterministic dispersion modeling for an urban operational scenario. In addition, the exponential value of the path loss at different UAV heights was calculated, as well as the distance–dependent path loss model and ray tracing estimates depending on the LOS and nonline–of–sight (NLOS) conditions.

In the literature, there has been a significant attention in UAVs and measurement campaigns including several modes and scenarios. Considering the transmission modes akin to terrestrial ones, A2G and A2A are the two prominent classes [8]. Among these two, A2A class needs further investigation due to the aforementioned reasons relevant to UAVs modes of operations [9, 10]. On the other hand, air–to–ground could be considered to be a transition class since it contains both terrestrial elements and UAVs simultaneously. Air–to–ground class consists of LOS, NLOS, and obstructed line–of–sight (OLOS) [11]. Of course, a comprehensive A2G model requires the probabilistic transitional states for LOS, NLOS, and OLOS cases to be defined as well [12–14]. It is obvious that further analysis is required to have an extended model which takes into account shadowing as an additional parameter [15–17]. A very detailed collection of studies present in the literature could be found in [18]. Beside statistical models which depend heavily on theoretical derivations [19], there are exact [20] and numerical approaches in determining the propagation characteristics as well. Especially ray tracing method that runs in downtown scenarios with the extension of building heights is employed very frequently [10, 21].

In the UAV–UAV channel model studies, results such as the received signal strength indicator (RSSI) of the signal using the 802.11–based UDP data and the packet loss are shown in [22]. EP–N8508GS 150 Mbit/s mini wireless 802.11n USB adapter is used with Raspberry Pi 3b on the receiver and transmitter sides. In addition, two VK2635U7G5LF GPS modules were used. In [23], a three-dimensional (3D) non–stationary geometry-based stochastic model (GBSM) is proposed for communication between UAVs.

For A2G propagation channels, in the literature, as mentioned above, there exists multiple studies covering both measurement and simulation-based models. [2] and references therein. In contrast, studies related to A2A channel modeling are limited. Hitherto A2A models are generally based on simulations [24]. In [25], an A2A channel model is provided for low altitude UAVs without considering channel characterizations in physical layer i.e., parameter extraction is carried out via user datagram protocol (UDP) packets. In [26], large–scale fading model between UAVs and base stations are studied for 800 MHz band. A recent study facilitates machine learning methods to predict path loss via ray tracing simulation software for A2A scenario [27].

In most of the channel modeling studies in the literature, simulation data are used instead of real field data, and it is seen that existing measurement studies are performed by using off–the–shelf products. Sufficient information was not given about the problems encountered in measurements made using off–the–shelf products on the shelf. For this reason, in Chapter 3, the problems arising in the measurements made by using a test setup using Software Based Radio USRP and a suitable antenna and amplifier have been studied. Despite the difficulties encountered, the reason why the USRP is preferred is that it is both lightweight and plug–and–play applicability and easily programmable. Although there are radio frequency (RF) products that are more successful than USRPs and provide solutions to problems such as center frequency shift, DC component and in–phase/quadrature (I/Q) imbalance at the hardware level, the reason why they are not preferred is because they are extremely complex programming structures and end–user products that are generally intended to meet a specific need. is that they cannot offer flexibility.

The conventional strategy to tackle the aforementioned utilization problem is reusing of resources as frequent as possible. Cell splitting, antenna sectoring, and small cell concepts are prominent examples to increase capacity via effective use of available bandwidth, reduce transmit power and impact of interference. There are products in the market regarding small cell (microcell, picocell, femtocell in the sense of metro femtocells, public access femtocells, enterprise femtocells and class 3 level femtocells, *etc.*) solutions which mainly rely on fixed deployment. However, with the emergence of UAVs, a paradigm shift has been experienced in wireless communication communities in many aspects. Considering its agility in 3D spatial domain and versatility in modes of operation, UAVs bring about almost a completely novel perspective in contemporary wireless mobile radio communication systems. Ranging from emergency communications to routing and relaying, UAVs are considered to be promising solution candidates in various wireless communication scenarios. In addition, the emerging concept of Internet of Things (IoT) mandates extending the wireless radio coverage to diverse (and relatively harsh propagation) environments. In the presence of such a vast variety of propagation environments, a successful wireless communication link depends on transceivers which rely on extended measurements and corresponding designs [28].

In the mission critical scenarios, where the utilization of UAV base stations (BSs)/access points (APs) such as disaster/public safety regions, rural areas and downtown areas where the total failure of communication infrastructure would lead to catastrophic events in terms of wireless communication, finding a rapid and cost–effective recovery solution that utilizes narrow band voice channels will be an important task. There have been some commercial services offered by cellular operators which claim to employ drones as hovering base stations in order to provide coverage in emergency scenarios and/or when disaster strikes. However, one of such operators which claimed to have UAV base stations could not provide service for a while after an earthquake of magnitude of 5.8 hit Istanbul, Turkey, on September 27th, 2020 [29]. This instance revealed that establishing communication via UAVs in a disaster scenario is a challenging task which has multiple dimensions including careful propagation channel analysis, detailed network planning, and spectrum management for first responders [30–32].

A critical factor in propagation modeling efforts is the overall cost and complexity of the campaigns for measurement–based studies. When UAVs are considered, extra constraints are imposed to measurements and traditional methods and equipment become inapplicable. For instance, vector network analyzer (VNA)–based channel sounding methods requires wiring between transmitter–receiver pair, which is not possible during measurement campaigns solely utilizing UAVs. Furthermore, VNAs are generally heavy-for UAVs to carry and quite expensive. Considering their limited payload and battery capacities of UAVs, utilizing software defined radio (SDR) solutions for propagation characterization is favourable. An example of an SDR–based channel sounding method is presented in [33]; for indoor environments.

Considering the contemporary A2A channel modeling activities and physical restrictions, first, an SDR-based channel measurement system is developed for A2A links of UAV to UAV wireless communications; a channel sounder at 5.8 GHz to capture A2A transmissions. Although over-the-air UAV communications exhibit many fundamental propagation behaviors, LOS large-scale characteristics are first to be analyzed considering the A2A UAV to UAV link topologies. To this end, an investigation of large-scale LOS channel characteristics is conducted through the estimation of path loss exponent using three different techniques. Thus, an accurate comparison of path loss exponent estimations which encompasses several path-loss modeling methods is provided.

2. CHANNEL MODELLING

2.1 Large-Scale Path Loss

Path loss refers to the reduction in power density (attenuation) of an electromagnetic wave as it propagates through space. For example, if there is 40 dB path loss in the system, a power level of -40 dbm is expected for 0 dbm transmission power. Factors affecting electromagnetic wave propagation are called reflection, refraction and scattering. Due to multipath reflections from different objects, electromagnetic waves travel by following different paths depending on varying distances. The interaction between these waves causes multipath attenuation at a certain point, and the amplitude of the waves decreases as the distance between the transmitter and the receiver increases. Despite the developed physical theories, it is difficult to predict the path loss. Various propagation models have been developed for this purpose. Propagation models are generally based on estimating the average signal level received at a particular point far from the transmitter. Propagation models based on randomly selected transmitter-receiver distance and estimating average signal strength are very important in calculating the transmitter coverage area. These models are known as large-scale propagation models because they describe the behavior of the signal intensity over large transceiver ranges, typically a few hundred or thousand meters. They are used to characterize the signal strength at different distances from the transmitter, taking into account factors such as the environment and the presence of obstacles.

2.1.1 Free space path loss

Free space path loss (FSPL) refers to the loss of signal strength that occurs as an electromagnetic wave propagates through free space (i.e., a vacuum). It is caused by the natural spreading of the wavefront and is proportional to the square of the distance between the transmitter and receiver. The power density of the wave (in watts per square meter) at a distance d from the transmitter can be calculated using the following equation:

$$S = \frac{P_t}{4\pi d^2} \tag{2.1}$$

where P_t is the power transmitted by the transmitter (in watts) and S is the power per unit area at distance. The factor of $4\pi d^2$ in the denominator represents the surface area of a sphere with radius d. Also, the receiving antenna's aperture, describes how well an antenna can pick up power from an incoming electromagnetic wave. For an isotropic antenna, this is given by

$$P_r = \frac{S\lambda^2}{4\pi} \tag{2.2}$$

where P_r is received power in watts and λ is the transmitted wavelength in meters. The free space path loss is given by the ratio:

$$FSPL = \frac{P_t}{P_r} = \left(\frac{4\pi d}{\lambda}\right)^2 \tag{2.3}$$

2.1.2 Path loss

Path Loss (PL) is a generalized form of FSPL. By using 2.1 and 2.2 received power is:

$$\begin{gathered} P_r = P_t G_t G_r \left(\frac{\lambda}{4\pi d}\right)^2 \\ PL(d) = \frac{P_t}{P_r} = \frac{1}{G_t G_r \left(\frac{4\pi d}{\lambda}\right)^2} \end{gathered} \tag{2.4}$$

where G_r and G_t are the gains of the receiver and transmitter antennas, respectively. For expressing in dB:

$$\begin{aligned} P_r(dB) &= P_t(dB) + G_r(dB) + G_t(dB) + 20\log_{10}\left(\frac{\lambda}{4\pi d}\right) \\ P_r(dB) &= P_t(dB) + G_r(dB) + G_t(dB) - 20\log_{10}\left(\frac{4\pi d}{\lambda}\right) \\ PL(dB) = P_t(dB) - P_r(dB) &= 20\log_{10}\left(\frac{4\pi d}{\lambda}\right) - G_r(dB) - G_t(dB) \end{aligned} \tag{2.5}$$

The majority of radio propagation models are created by combining analytical and empirical methodologies. Fitting curves or mathematical formulae to reproduce a collection of observed data is the empirical technique. In addition, the empirical approach makes it possible to indirectly consider all the propagation parameters that may occur with the real field measurements. However, additional observed data in the new condition at the requisite communication frequency is required to verify the effectiveness of an empirical model at communication frequencies or settings different than those used to create the model. Over time, a number of classic propagation models have been developed to predict the coverage and signal-to-noise ratio (SNR) of mobile communication systems. These models are used by engineers to design and optimize the performance of such systems. For example, the two-ray model is a classic propagation model that was used to estimate the spread spectrum system capacity before it was deployed. This model takes into account the distance between the transmitter and receiver, as well as the environment and other factors, to predict the received signal intensity and overall system performance. These models are important for ensuring that mobile communication systems have adequate coverage and signal quality.

In addition to the two-ray model, there are many other classic propagation models that are used in mobile communication system design. These include the free-space model, the log-distance model, the Hata model, and the Okumura-Hata model, among others. Each model has its own strengths and limitations, and the appropriate model to use depends on the specific characteristics of the communication system and the environment in which it will be deployed. These models are typically validated through field measurements and simulations to ensure their accuracy and reliability.

2.1.2.1 Log-distance path loss model

Path loss models have been widely used in the literature and can be derived from theoretical or measurement-based approaches. The average large-scale path loss is expressed using a path loss exponent, n, which represents the rate at which the signal strength decreases as distance increases. The value of n is determined by the propagation environment and is typically 2 in free space but can be higher in environments with obstructions or other factors that can affect the signal. Accurate predictions of path loss require choosing a suitable reference distance for the given propagation environment. These models are commonly used in wireless communication systems to predict the signal strength at a given distance.

$$\begin{gathered}\overline{PL}(d) \propto \left(\frac{d}{d_0}\right)^n \\ \overline{PL}(\text{ dB}) = \overline{PL}(d_0) + 10n\log\left(\frac{d}{d_0}\right)\end{gathered} \qquad \textbf{(2.6)}$$

where n denotes the path loss exponent, which represents the rate at which path loss grows as distance increases and the close-in reference distance, d_0, is calculated using measurements taken closer to the transmitter, and d is the Tx-Rx separation distance. The bars in for a given value of d, equation 2.6 signifies the average of all possible path loss values The predicted path loss follows a linear relationship with a slope of $10n$dB per decade when plotted on a log-log scale. The value of n is determined by the propagation environment. In free space, for example, n equals 2, but when obstructions are present, n increases. It's critical to choose a free space reference distance that's suitable for the propagation environment. 1km reference lengths are often employed in high coverage cellular systems, although significantly shorter distances (such as 100m or 1m) are utilized in microcellular systems. To avoid the influence of near-field effects on the reference path loss, it is important to ensure that the antenna is in its far field region when the reference distance is chosen. This will ensure that the reference path loss is not affected by near-field effects and that the predictions of path loss are accurate. By carefully selecting the reference distance and operating the antenna in its far field region, we can improve the accuracy and reliability of the path loss measurements and model. In other words, the reference distance should be sufficiently far away from the antenna so that the near-field effects are negligible.

2.1.2.2 Log-normal shadowing

Equation 2.6 ignores the reality that the surrounding environmental clutter at two distinct positions with the same Tx-Rx separation may be drastically different. The observed signal strength at a given site deviates significantly from the average value predicted by the log-distance path loss model. This is because the path loss at a given site is random and follows a log-normal distribution around the mean distance-dependent value. In other words, the path loss at a given distance is not always exactly the same and can vary from the average value predicted by the model. This is confirmed by measurements of the signal strength at various distances from the transmitter. That is

$$PL(d)[dB] = \overline{PL}(d) + X_0 = \overline{PL}(d_0) + 10n\log\left(\frac{d}{d_0}\right) + X_\sigma \qquad \mathbf{(2.7)}$$

The random shadowing effects that occur over many measurement locations with the same transmitter-receiver separation but different amounts of clutter on the propagation path are described by a log-normal distribution. This is known as log-normal shadowing. In other words, the observed signal levels at a given transmitter-receiver distance have a Gaussian distribution around the mean that depends on the distance, with measured signal levels in decibels (dB). The standard deviation of the Gaussian distribution representing shadowing is also expressed in dB. The random variable describing shadowing is given by X_σ, where σ is the standard deviation of the Gaussian distribution in dB. This equation can be expressed as:

$$X_\sigma \sim \mathscr{N}(0, \sigma^2) \tag{2.8}$$

where $\mathscr{N}(\mu, \sigma^2)$ denotes a normal distribution with mean μ and variance σ^2. The Gaussian distribution is used to model the random effects of shadowing and can be easily analyzed. The path loss model for a specific transmitter-receiver separation is statistically described by the close-in reference distance d_0, the path loss exponent n, and the standard deviation σ. This model can be used in computer simulations to generate received power levels for random locations in communication system design and analysis. In practice, the values of n and σ are calculated from observed data using linear regression, with the goal of minimizing the mean square error between the measured and predicted path losses across a range of measurement locations and transmitter-receiver separations.

2.2 Small-Scale Fading and Multipath

Small-scale fading, or fading, refers to the fast variations of a radio signal's amplitudes, phases, or multipath delays over a short period of time or travel distance. This type of fading is caused by interference between two or more copies of the transmitted signal arriving at the receiver at slightly different times. These waves, known as multipath waves, combine at the receiver antenna to produce a signal with a range of amplitudes and phases. The exact distribution of these amplitudes and phases depends on the intensity of the waves and their relative propagation times, and the transmitted signal bandwidth. This thesis does not investigate small-scale fading but instead focuses on large-scale characteristics of the signal.

2.2.1 Small-scale multipath propagation

Small-scale fading is a result of multipath in the radio channel. Multipath occurs when multiple copies of the transmitted signal arrive at the receiver at slightly different times, interfering with each other. These interfering waves combine to create a signal with varying amplitudes and phases, depending on the intensity and relative propagation times of the waves. This phenomenon is known as small-scale fading and can affect the performance of wireless communication systems. To mitigate the effects of small-scale fading, communication systems frequently employ methods such as diversity or error correction codes to improve the reliability of the received signal. The following are the three most significant factors:

- Rapid variations in signal intensity over a short travel distance or time interval
- Random frequency modulation because of differing Doppler shifts on separate multipath signals
- Multipath propagation delays generate time dispersion (echoes)

Fading happens in densely populated areas because there is not a single route that provides a direct line of sight to the base station. This is because the height of mobile antennas is much lower than the height of the surrounding buildings. Due to reflections off the ground and other objects, multipath may occur even when there is a direct line of sight between two points. Because radio waves travel in all directions, the time it takes for them to arrive at their destination might vary significantly. At each point in space, the mobile device has the potential to pick up a huge number of plane waves with amplitudes, phases, and angles of arrival that are all randomly scattered over the spectrum. These multipath components collect vector when they reach the receiving antenna, which causes the signal resulting in fading or deterioration of the signal received by the mobile device. Even if a mobile receiver is kept in a fixed position, there is still a chance that the received signal may weaken because of the movement of surrounding objects that are inside the radio channel. Fading in a radio channel can be a spatial event, where the receiver experiences changes in the signal while traveling through the multipath environment. This can cause the receiver to go through multiple fades in a short period of time, and in severe cases, the received signal may be stuck in a state of severe fading, making communication difficult. Antenna space diversity can reduce the effects of deep fading nulls from occurring by decreasing the likelihood of the received signal staying in a deep null for an extended period of time. For the most part, fading is a spatial phenomenon that happens when everything in the radio channel remains still except for the receiver. As a signal travels through a multipath

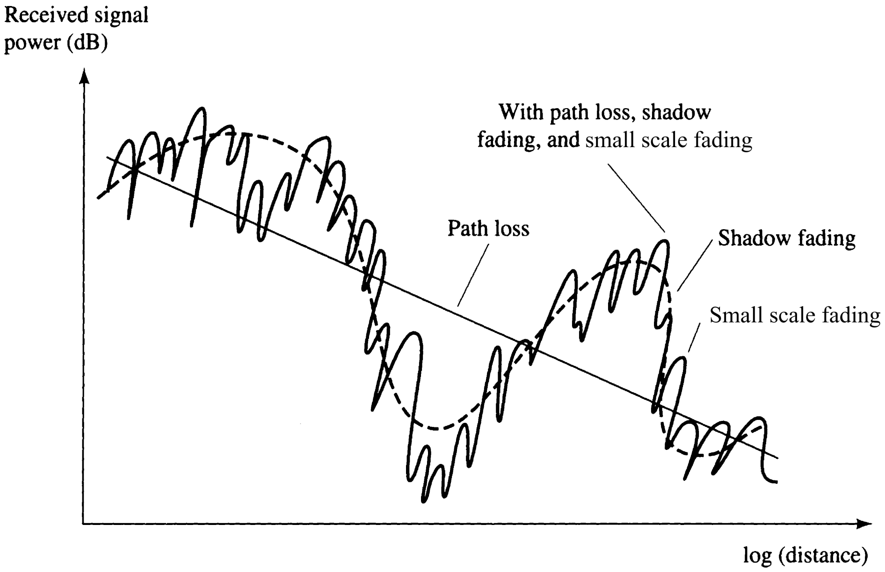

Figure 2.1 : Path loss, shadowing and small scale fading is varying over distance.

environment, the receiver will experience what seem to be temporal fluctuations due to the spatial changes in the received signal. The constructive and destructive actions of multipath waves at distinct sites might cause a receiver traveling at a high speed to experience many fades in a very short amount of time. It is possible for a receiver to get stuck in a region with very weak signal strength. Although the movement of surrounding things like automobiles or people may disturb the field pattern and lessen the possibility of the receiver being in a deep null for a lengthy amount of time, this can make maintaining excellent communication challenging. Deep fading nulls may be avoided with enough antenna diversity. Small-scale fading, as seen in Figure 2.1 [34], causes rapid variations in the strength of the received signal when the receiver travels across only a few meters in distance. Because of the movement of the receiver and transmitter relative to each other, the apparent frequency of each multipath wave is different. Doppler shift describes this change brought on by the receiver's own velocity. When a multipath wave is received, its Doppler shift is dependent on the receiver's speed and the direction of motion with respect to the multipath wave's direction of arrival. Doppler shift is essential in radar and navigation for calculating the relative velocity between a sender and a receiver. It helps determine the speed at which an object is moving in relation to an observer, allowing accurate radar measurements and precise navigation calculations. By analyzing the frequency shift caused by the

Doppler effect, valuable information about the object's motion, including speed and direction, can be obtained.

2.2.2 Time dispersion characteristics

The multipath channel is characterized by a number of parameters that are used to evaluate different multipath channels and provide basic design principles for wireless systems. These metrics, such as mean excess delay, RMS delay spread, and excess delay spread (X dB), are calculated using a power delay profile. The mean excess delay and RMS delay spread are often used to measure the temporal dispersive properties of wideband multipath channels. The mean excess delay is the first moment of the power delay profile, while the RMS delay spread is the second central moment of the power delay profile. These delays are measured from the time that the first discernible signal reaches the receiver. In outdoor mobile radio channels, the RMS delay spread is typically on the order of microseconds, while indoor radio channels have RMS delay spread on the order of nanoseconds.

To obtain a statistical description of the multipath channel over a large area for a mobile communication system, multiple measurements are taken at many small locations. This allows the calculation of the RMS delay spread and mean excess delay using a single power delay profile, which is the temporal or spatial average of sequential impulse response measurements collected and averaged over a limited region.

The maximum excess delay (X dB) of the power delay profile is the time delay during which multipath energy decreases to X dB below the maximum. The maximum excess delay (X dB) indicates the temporal extent of the multipath over a certain threshold.

It is important to note that the Fourier transform relates the power delay profile and the magnitude frequency response of a mobile radio channel. By analyzing the channel's frequency characteristics, an equivalent frequency domain representation of the channel can be obtained. The coherence bandwidth is used to characterize the channel in the frequency domain, in a manner similar to the delay spread parameters in the time domain. The relationship between RMS delay spread and coherence bandwidth varies depending on the specific multipath topology. However, in general, these two parameters are inversely proportional to each other. This means that as the RMS delay spread increases, the coherence bandwidth decreases, and vice versa.

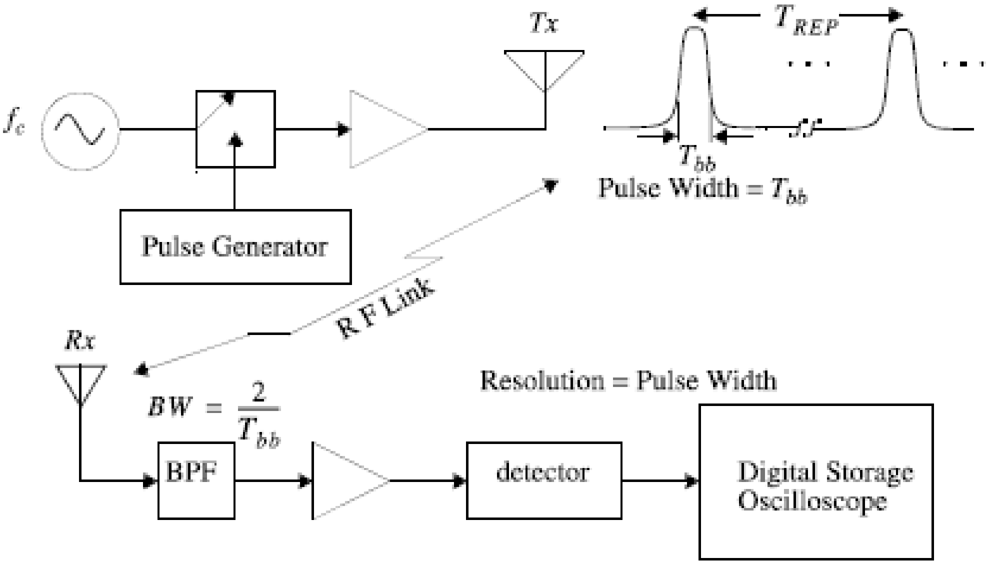

Figure 2.2 : Direct RF pulse measurement system.

2.3 Channel Sounding Methods

There are many channel sounding methods have been specified in the literature. A few main methods will be discussed in this section.

2.3.1 Direct RF pulse system

The direct RF pulse system (see Figure 2.2 [35]) is a simple channel sounding technique. As proved by Rappaport and Seidel, this approach facilitates quick calculation of the power delay profile for any channel by engineers. This technology, which is essentially a wideband pulsed bistatic radar, sends out a T_{bb}s wide repeated pulse and employs a receiver with a wide bandpass filter. An envelope detector detects the signal, which is subsequently displayed and recorded on a high-speed oscilloscope. The square of the channel impulse response is combined with the probing pulse through convolution, and the resulting output is immediately measured. This system may produce a local average power delay profile if the oscilloscope is set to an averaging mode. Another appealing feature of this system is its simplicity, as off-the-shelf equipment may be employed.

2.3.2 Sliding correlator channel sounding

A sliding correlator channel sounding system is a technique used to measure the characteristics of a wireless communication channel, such as its impulse response or

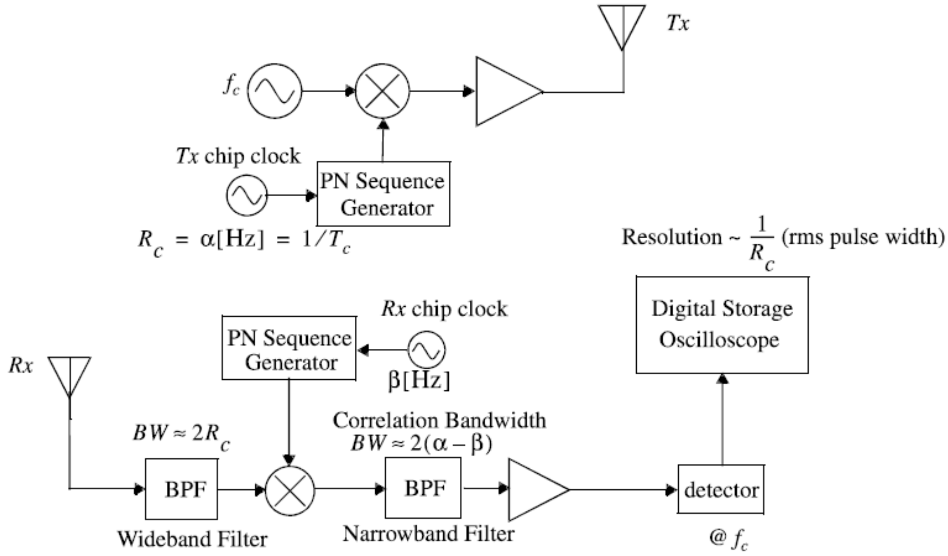

Figure 2.3 : Spread spectrum sliding correlator channel sounding measurement system.

frequency response. In this system, the transmitter uses a spreading signal, typically a pseudo-random noise (PN) sequence, to spread the signal over a wide bandwidth. This spreading allows the signal to be transmitted over a wide frequency range, which improves the dynamic range and sensitivity of the receiver.

At the receiver, a similar PN sequence is used to despread the signal and recover the original data. The receiver chip clock is typically slightly slower than the transmitter chip clock, which creates a "sliding" effect between the two PN sequences. As the transmitter chip clock catches up to the receiver chip clock, the two PN sequences will be almost exactly matched, resulting in maximum correlation. This allows the receiver to filter out unwanted signal power and noise, improving the signal-to-noise ratio.

The block design of a sliding correlator channel sounding system is illustrated in the following figure:

In Figure 2.3 [35], the transmitter generates a spreading signal, typically a PN sequence, and mixes it with the data signal to spread the signal over a wide frequency range. At the receiver, the incoming spread spectrum signal is mixed with a similar PN sequence to despread the signal and recover the original data. The receiver chip clock is slightly slower than the transmitter chip clock, which creates the sliding effect between the two PN sequences. When the two PN sequences are almost exactly matched, the maximum correlation is achieved, which allows the receiver to filter out unwanted signal power and noise.

In summary, a sliding correlator channel sounding system employs a clever technique known as a spreading signal, which enables the transmission of signals across a wide frequency range. At the receiver end, a corresponding pseudo-noise (PN) sequence is utilized to efficiently extract the original data while effectively suppressing unwanted signal power and mitigating the impact of noise. This innovative approach brings about notable benefits, such as enhancing the dynamic range and sensitivity of the receiver, thus surpassing the capabilities of a conventional direct RF pulse system. By leveraging the sliding correlator technique, the system achieves improved signal fidelity and greater resilience to interference, resulting in enhanced overall performance and reliability.

2.3.3 Frequency domain channel sounding

The channel transfer function (CTF) is computed in the frequency domain using the frequency hopping (FH) approach. As excitation, the Tx uses a variation narrowband signal: a sinusoidal signal with constant peak amplitude but discrete frequency changes at predetermined time intervals. The sequence is also known by the receiver. It determines the amplitude of the received signal for each specific frequency and then calculates the CTF throughout the frequency range based on the transmitted signal [36]. A frequency domain sounder is a tool that enables detailed analysis of wideband channel propagation statistics, such as delay spread, power delay profiles (PDPs), and correlation bandwidth. This sounder can also be used to study the frequency selectivity of channels using a swept-frequency channel sounder.

3. DEVELOPMENT OF THE SOFTWARE DEFINED RADIO BASED CHANNEL MEASUREMENT SYSTEM

In this section, the measurement campaigns created for UAV channel modeling, the difficulties encountered and the solutions brought to them will be discussed. While designing measurement campaigns, structures and updates that change over time will be explained separately.

3.1 Challenges Encountered in Measurements

3.1.1 Difficulties in hardware

In this section, general definitions and results of regarding the center frequency shift, local oscillator (LO) leakage, I/Q imbalance, harmonics and undesired signals observed in the measurements made with the USRP B210 and the efforts to correct them will be examined.

3.1.1.1 Center frequency offset

Local oscillator LO is used in conjunction using a mixer to shift the frequency of a signal. The process of frequency conversion, also known as heterodyning, involves combining the input signal's frequency with that of a LO to generate new frequencies that are the sum and difference of the two. This process allows for the manipulation and analysis of the input signal in various ways. Oscillatory crystals are not perfect because they do not oscillate at the exact specified frequency. Due to defects and tolerances in the manufacturing process, oscillatory crystals typically have 20 or 50 parts per million (ppm) defects guaranteed by the manufacturer. These values are at the level of about ±2 ppm in USRP E312 [37] and B210 [38]. Even relatively small differences in the center frequency in the communication traffic between the transmitter and receiver can prevent the receiver from decoding the transmission. In eliminating the central frequency shift problem, devices such as USRP provide a solution to the specified problem by providing clock source input. Also, one way to solve the center frequency shift can be achieved by connecting the frequency synchronization between the transmitter and receiver to the common clock output.

In the first test scenario related to the center frequency shift, a sample of 200000 was taken with 200 kHz sampling rate in the 5.8 GHz frequency band, which was considered for B210 UAV channel measurement studies, and a single tone was sent and recorded with the help of Rohde & Schwarz FSW26 Signal Analyzer. Then, the recorded signal is processed with the help of Matlab and the center frequency shift is corrected. The results are given in Figure 3.1.

Since the center frequency of the signal sent in the measurement scenario considered for channel measurements is known, the shift of the observed center frequency in the received signal is determined by calculating the difference between them. When the determined difference is multiplied as a complex signal in the time zone, it is shifted by the error in the frequency zone and the center frequency is pulled to where it should be. As an alternative way, as stated in Section 3.1.1.1, it shows an error in the range specified in the data sheet of the device as the frequency shift is due to LO and occurs depending on the device. This value is a fixed value for the device, and the offset values can be predetermined depending on the frequency. Accordingly, the center shift is corrected according to the value found.

3.1.1.2 Leakage in center frequency components

If the RF signal is hit with the carrier in the receiver, the RF signal will return to the baseband (BB). In this process, center frequency components go to DC (0 Hz) in BB, which can saturate the low noise amplifier (LNA) or receiver components or affect receiver performance. This situation can also be expressed in terms such as carrier suppression, LO leakage, DC leakage and center frequency leakage. Local oscillator leak, transmitted uncorrected, causes unwanted emissions in transmission. Because the unwanted component in the multiplication process occurs due to the deficiencies in its mixer structure. Ideal mixers have two input ports and one output port. The ideal mixer produces an output that is the product of two inputs. In terms of frequency, the output to be generated should be $F_{input} + F_{LO}$ and $F_{input} - F_{LO}$ [39]. If F_{input} is considered for the case of 1 MHz, the baseband frequency will be F_{BBand} and in the case of a 5800 MHz LO, the frequency will be F_{LO}. is set. Ideally, a mixer would produce two tone signals at the output, one at 5799 MHz and the other at 5801 MHz. However, in

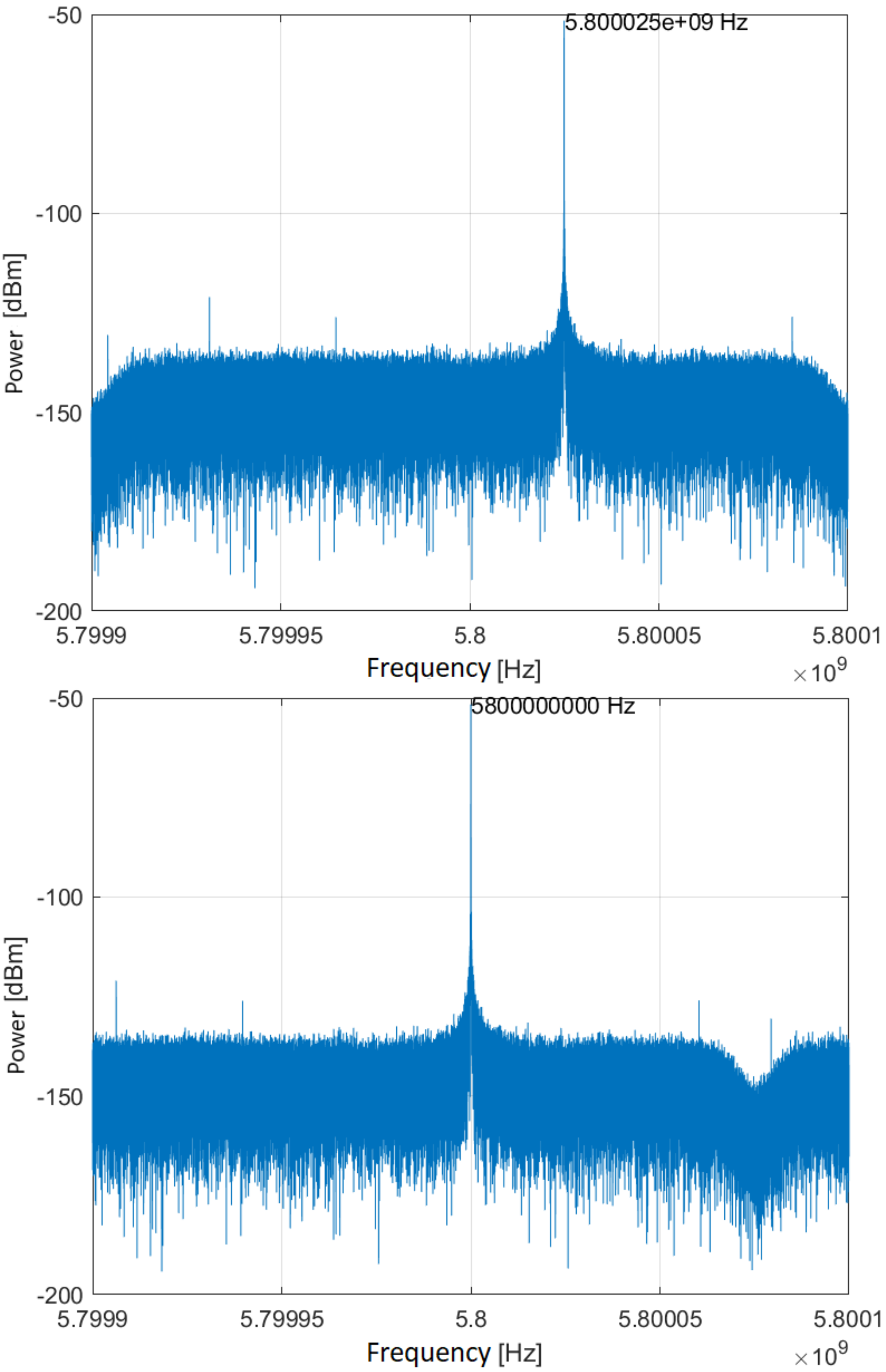

Figure 3.1 : Center frequency offset signal recorded in the 5.8 GHz frequency band and corrected signal.

practice, a mixer will generate some energy at F_{BBand} and F_{LO}. The energy at F_{BBand} is usually insignificant because it is far from the intended output and can be filtered out by the RF components downstream of the mixer. This energy can be ignored because it does not affect the performance of the mixer. However, the energy at F_{LO} must be carefully managed to avoid degrading the performance of the mixer. This energy is problematic because it is close to or within the intended output signal, and it is difficult or impossible to remove by filtering without also affecting the desired output. The energy at F_{LO}, however, can be problematic. F_{LO} is close to or inside the target output signal and cannot be easily removed by filtering without also removing the target signal. F_{LO} is called the local oscillator leak (LOL) and is unwanted energy. It arises from the local oscillator (LO) driving the mixer leaking to the mixer's output port. In an intermediate frequency (IF) architecture that only transmits one sideband, the LOL can be addressed using radio frequency (RF) filters. In a zero-IF architecture that transmits both sidebands, the LOL is positioned at the center of the target output, making it more challenging to manage. Unlike in a traditional intermediate frequency (IF) architecture where only one sideband is transmitted, filtering is no longer an effective solution because it would also remove part of the desired transmission. To avoid this issue, new methods must be used to prevent the inclusion of the LOL in the transmission, otherwise, the intended transmission may be contaminated with an unwanted broadcast signal. In the simulation studies related to DC offset, DC component removed with the DC Blocker block provided by GNURadio software with the observed DC component at 5.8 GHz center frequency with 10 MHz sampling rate and 4096 FFT rate when the USRP B210 device is used as a receiver in tests related to DC leakage is shown in Figure 3.2.

3.1.1.3 Inphase/Quadrature imbalance

Direct conversion receivers that use in-phase/quadrature (I/Q) processing have become increasingly popular in recent years because they offer a simpler and more cost-effective alternative to superheterodyne architectures [40]. In principle, these receivers have the advantage of not requiring image filtering to remove the image band. However, in practice, it is difficult to achieve the two conditions necessary for the complete removal of the image band: (1) the LO must generate signals that are phase-shifted by exactly ± 90 degrees, and (2) the I and Q branches must have matched gains and phase responses. In reality, analog components often have imbalanced gain and phase responses, which makes it impossible to fully remove the image band [41]. Ideally, the receiver's I and Q outputs could be expressed as $I(t) = \cos(\omega t)$ and $Q(t) = \sin(\omega t)$. Here ω represents the baseband frequency of the tone signal. Typical

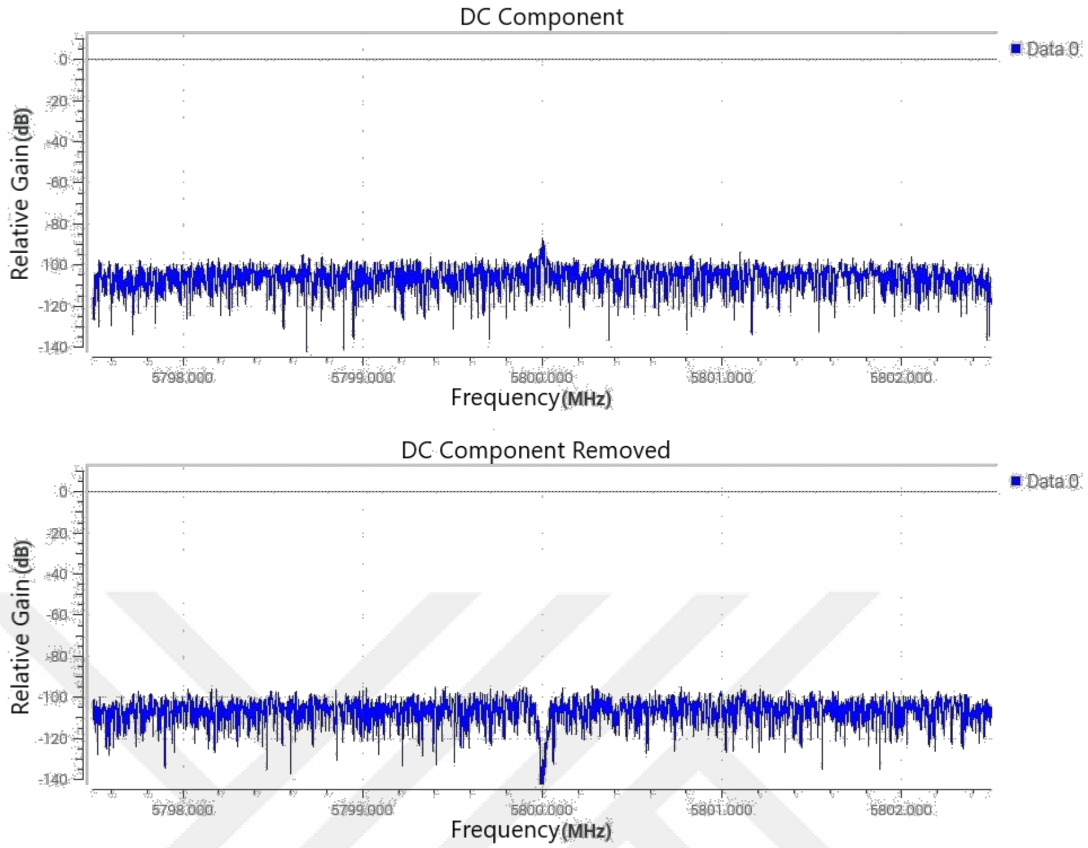

Figure 3.2 : The signal on the receiver where the DC component is observed and the signal that occurs after the DC component is removed.

erroneous I and Q values in direct conversion system receivers can be expressed as:

$$I^I(t) = \alpha\cos(\omega t) + \beta_I,\ Q^I(t) = \sin(\omega t + \delta) + \beta_Q \tag{3.1}$$

δ, phase error due to Q component; α denotes the amplitude error caused by the I component, and β_I and β_Q denote the DC component for each path. Averaging $I^I(t)$ and $Q^I(t)$ over a period to remove β_I and β_Q components from given paths is enough. In this case, I'' and Q'' expressions remain and this expression can be expressed in matrix format as follows;

$$\begin{bmatrix} I^{II}(t) \\ Q^{II}(t) \end{bmatrix} = \begin{bmatrix} \alpha & 0 \\ \sin(\delta) & \cos(\delta) \end{bmatrix} \begin{bmatrix} I(t) \\ Q(t) \end{bmatrix} \tag{3.2}$$

The expression is obtained using the equation $\sin(wt+\delta) = \sin(\omega t)\cos(\delta) + \cos(\omega t)\sin(\delta)$. The following expression can be obtained as a result of rearranging the obtained matrix to reach the smoothing matrix:

$$\begin{bmatrix} I(t) \\ Q(t) \end{bmatrix} = \begin{bmatrix} \alpha^{-1} & 0 \\ \alpha^{-1}\tan(\delta) & \sec(\delta) \end{bmatrix} \begin{bmatrix} I^{II}(t) \\ Q^{II}(t) \end{bmatrix} \tag{3.3}$$

So it is necessary to find the terms α ve δ to solve the equation. The following expression can be used to find α':

$$< I^{II}(t)I^{II}(t) >= \quad \alpha^2 \left\langle \tfrac{1}{2} + \tfrac{1}{2}\cos(2\omega t) \right\rangle = \tfrac{1}{2}\alpha^2 \tag{3.4}$$

(3.4) after rearranging the expression, the following expression can be obtained:

$$< I^{II}(t)Q^{II}(t) >= \frac{1}{2}\alpha^2 \sin(\delta) \tag{3.5}$$

statements can be written. Therefore, using Equation **(3.4)**, α and Equation **(3.5)** are used to find $\sin(\delta)$. Also, assuming $|\delta| < \pi/2$, which is provided for any phase imbalance, the expression $\cos(\delta)$ can be derived directly from the expression $\sin(\delta)$. In summary, solving the following matrix equation will correct the I/Q imbalance:

$$\begin{bmatrix} I(t) \\ Q(t) \end{bmatrix} = \begin{bmatrix} A & 0 \\ C & D \end{bmatrix} \begin{bmatrix} I^I(t) - \beta_I \\ Q^I(t) - \beta_Q \end{bmatrix} \tag{3.6}$$

where $A = 1/\alpha$, $C = -\sin(\delta)/(\alpha\cos(\delta))$ and $D = 1/\cos(\delta)$ are denoted.

In addition to the problems caused by the specified USRP hardware, oscillations were observed while the amplitudes of the sent channel sounding signals were expected to be constant. In the simulation studies related to I/Q imbalance, the results obtained in the test scenario created with 200 kHz sampling rate in Matlab environment are shown in Figure 3.3. The I and Q signals produced are broken in line with the parameters $\alpha = 5$, $\delta = \pi/5$ and $\beta_I = 2.5$, $\beta_Q = 4$ and Figure 3.3 It is corrupted as in the second graph in. The third graph is obtained by inserting the broken signal into the correction algorithm as explained in the section 3.1.1.3. Another point to note here is that the generated signal is valid under the assumption of a linear time invariant signal (LTI). Different solutions have been developed for I/Q correction in systems that change over time. One of them is demonstrated using the feed forward correction method in the I/Q correction model of Moseley [40]. In addition, as a more advanced method, an adaptive algorithm using Antilla [42] second order I/Q statistics is proposed.

3.1.2 Amplifier, converter, power supply, GPS module and raspberry pi 4b

3.1.2.1 Amplifier selection

While designing the UAV channel measurement system, an amplifier was used to strengthen the signal from the USRP. One thing to note here is how much gain will

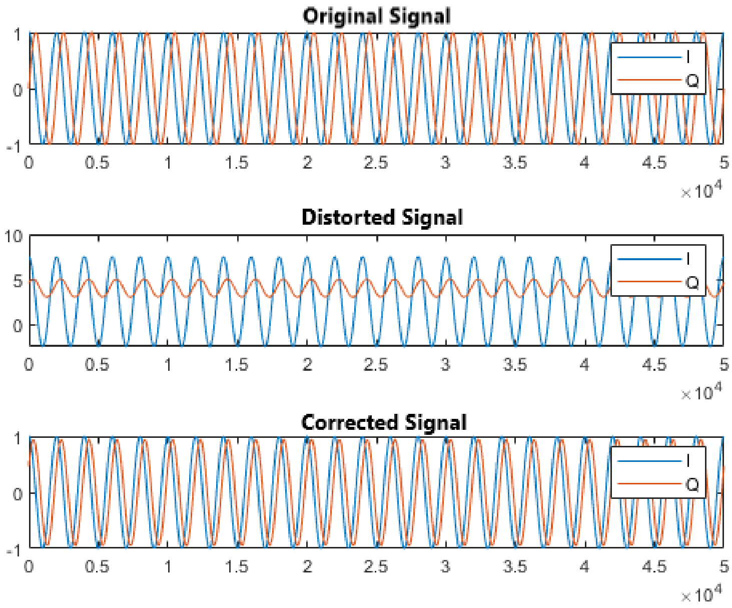

Figure 3.3 : Created, distorted and corrected signal to indicate I/Q imbalance.

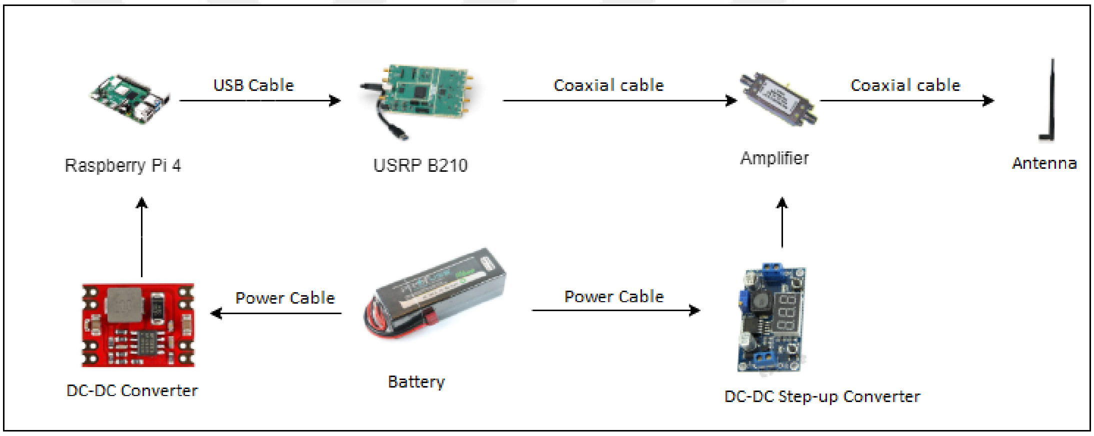

Figure 3.4 : Transceiver block diagram for channel modeling.

be provided in the frequency band to be studied. The amplifier shown in Figure 3.4 operates in the $2-18GHz$ band and gains 32 decibel(dB). Although it consumes about 280 mA as power consumption, it requires a power supply in the range of $12-15V$. Since it does not have a separate cooler structure on it, an additional cooler was added to the riser.

3.1.2.2 Power supply

A 11.1 V Lithium-Polymer (Li-Po) battery with a 6000 mAh capacity is used as the power source of the system. The reason why such a battery is preferred is that it allows high current to be drawn and offers long-term use.

3.1.2.3 DC-DC converter selection

Since the measuring system operates with its own power source independent of the environment, it is necessary to feed the system with a single power source. It is a amplifier with Raspberry Pi 4 fed directly from the power supply, but DC - DC converters are needed because the power they draw and the voltage ranges they operate are different. For this reason, since Raspberry Pi 4B operates at 5.1 V and draws up to 3 A current, a DC - DC step–down converter circuit that drops it to 11.1 V at 5 V is used. In addition, since the amplifier operates at the previously specified voltage values, a DC - DC step–up converter circuit has been used. Another point that should be considered here is that the converters must be resistant to the maximum current drawn by the devices specified, and the maximum current capacity of the converters must be a certain amount above the maximum current level that the devices will draw.

3.1.2.4 GPS module

Since the measurement system will be on the UAVs, the U-Blox Neo 7m GPS module was used to detect the measurement points made. It has been tried to communicate with Raspberry Pi 4 via serial port by connecting it with pin outputs on it.

3.1.2.5 Raspberry pi 4b

The Raspberry Pi 4B 4GB model has been used to control the USRP, to power the USRP, to communicate with the GPS module and to control the measurement system remotely. It is used because of its features such as its lightweight structure, powerful processor, wireless dual band operation (2.4 and 5 GHz), and Bluetooth support, and having an open source Linux distribution. That is why this device has been chosen as the brain of the measuring system.

3.1.3 Challenges on the software and algorithm side

Two methods have been considered for channel measurements. The first is Channel Sounding method. The impulse response of the channel is extracted as a result of the correlation process with the same random sequence in the receiver by sending signals from the transmitter with the help of a random array of a certain length. Correlative sequences can be binary or non-binary. Typical binary arrays are so-called noise sequences. Generally, maximum length sequences are used for this purpose.

Arrays of different length have been tried in the measurement studies. It is also available in specially designated series. One of them is the Gold series used by LTE. Due to the oscillations in the peaks caused by the correlation in USRP, the desired impulse responses could not be achieved with this method. In the second method, the frequency impulse response of the channel is extracted by shifting the frequency at certain intervals in the specified frequency band. When the correlation sequence method was not successful, the frequency impulse response of the channel was found by shifting the frequency. A suitable measurement scenario has been created by testing different frequency ranges in different frequency bands. During the tests, the duration of each slip caused by the LO in the USRP was tried to be optimized. GNURadio, an open source software based radio programming tool, is used to control USRP. UHD software has been installed for the drivers of the USRP. To control the GPS module, GPSD service has been installed and the necessary parameters have been entered and communication with the GPS module has been provided. In addition, GPS data was recorded with the received signal to determine the location of the point taken in the measurements. In order to connect to Raspberry Pi while on UAV, remote access is provided with iPad.

3.2 Measurement Campaign and Measurement Setup for Air–to–Ground

- **Location:** The measurements are collected in the test field which is shown in Figure 4.3(b) of The Scientific and Technological Research Council of Turkey (TUBITAK) in Gebze.

- **Transmitter:** The signal is a PN-sequence with a length of 4095 and it is transmitted with 30 dBm power in 446 MHz center frequency on the UAV side..

- **UAV:** DJI Matris 600 Pro is flied up to obtain measurement and it is used as a air station since its payload capability and durability in extreme conditions. It is shown in Figure 4.3(a).

- **Receiver:** On the other hand, a channel sounder in Figure 4.1, is used as a ground station to receive the transmitting signals. It is configured in center frequency 446 MHz and 50MHz bandwidth for receiving PN-sequence signals.

- **I/Q Record:** All receiving signals are recorded with a period of 100 ms on an SSD which supports high-speed data transmission.

- **Antenna:** Furthermore, a monopole antenna which a frequency range from 400MHz to 470MHz is used for the ground station to receive the signals. The antenna has an omnidirectional radiation pattern and it has 3.3dBi antenna gain at 433MHz.

- **Results:** After the calculation of received powers of each point, then path loss model are extracted as it will be explained in Section 4.3.

3.2.1 Measurement methodology air–to–ground

- All the field measurements are conducted in the 446 MHz frequency band by using a channel sounder developed by HİSAR Lab. attached to a commercial UAV and all the signals are captured by the ground station with 50 MHz bandwidth.

- The measurements are collected from 60m to 80m heights with step size 10m vertically.

- **Height limitation:** Local regulations allow UAV to operate up to 120m in height, however, due to the topographical conditions and the high wind speed after 80m in height, measurements are performed for 60m to 80m in height.

- **Flight regulations:** Moreover, the only allocated location for UAV flight is, where the measurement is taken, is shown 4.3(b) in TUBITAK, Gebze.

- Also, for each vertical measurement point, UAV move between 10m to 410m horizontally. The overall grid consists of total of 800 determined location points with 60m to 80m vertically and 10m to 400m horizontally.

- Both the transmitting and receiving Software-Defined Radios (SDRs) within the system are meticulously synchronized using a highly accurate 10 MHz clock signal sourced from a Global Positioning System Disciplined Oscillator (GPSDO). This synchronization ensures precise alignment between the transmitter and receiver, facilitating seamless communication and minimizing timing discrepancies. Additionally, the GPS receiver integrated into the system provides exceptional levels of accuracy in determining the geographic location, enabling the transceivers to leverage high-precision location measurements for various applications. By harnessing the power of this synchronized setup and leveraging the precise location data provided by the GPS receiver, the system attains superior performance, robustness, and reliability in wireless communications.

3.3 Measurement Setup for Air–to–Air

3.3.1 Measurement environment

- **Antenna test:** To verify antenna pattern and free space path loss performance, a measurement setup is constructed in the Antenna Test and Research Laboratory (ATAM) of TUBITAK BILGEM as shown in Figure 5.1(a). The dimensions of the anechoic chamber is 17 m × 18 m× 14 m (L×W×H) and frequency range is 0.5 GHz – 40 GHz.
- **Location:** Field measurements are taken at the TUBITAK BILGEM Gebze campus (as shown in Figure 5.1(b)) which consists of a rural area with trees causing ground reflection signal to drastically lose its power, hence the reflected signal power falls below the noise level.
- **Path:** The location of the stationary receiver and the route followed by the transmitter during the measurement on a 3D map are also exhibited in Figure 5.1(b).

3.3.2 Measurement equipment

- **UAVs:** As shown in Figure 5.2, two identical DJI Matrice 600 Pro hexacopter drones are used as receiver and transmitter.
- **Measurement Box:** The channel measurement box contains the TX and RX modules are attached to drones.
- **Transceivers:** Each TX and RX channel measurement box consist of one bladeRF 2.0 micro xA9 transceiver,
- **Amplifiers:** a Lucix S020180L3205 RF power amplifier to boost signal for both side,

Figure 3.5 : Illustration of the measurement campaign in which two commercially available hexacopter are used as transmitter and receiver. Note that two drones are ready to take–off with mounted channel measurement box.

- **Mini Computer:** as a mini-computer Raspberry Pi 4B,
- **Antenna:** circularly polarized (CP) antenna which Antenna radiation pattern is shown in Figure 5.3 The coupling effect of the drone on the radiation pattern of the antenna is analyzed, and in this regard, the measurements are taken under the presence and absence of the drone at the anechoic chamber. It can be seen that the coupling effect of the drone can be considered negligible level as shown in Figure 5.3(a) and Figure 5.3(b) for elevation and azimuth directions, respectively and
- **Power:** 28 600 mA h powerbank which has high current capability is used as battery.
- **Remote Computer:** Also an Android cellular phone is utilized to control both Raspberry Pi 4 from the ground.
- **Measurement system:** The measurement system block diagram is depicted in Figure 5.4 and channel sounding equipment is given in Figure 5.5. Note that back–to–back calibration is employed with RF cable connections so that the impairments stemming from the aforementioned devices are compensated.

3.3.3 Measurement methodology

The measurement experiments are firstly performed in Anechoic chamber measurements are taken for separation distances of 1 m, 2 m, 3 m and 4 m, respectively as seen in Figure 5.1(a) and secondly real-world measurements:

Table 3.1 : Measurement Parameters.

Parameter	**Symbol**	**Value**
Sample Rate	f_s	8 MHz
Start Frequency	f_{start}	5.820 45 GHz
Stop Frequency	f_{stop}	5.827 55 GHz
Discrete Sweep Step Interval	Δf	50 kHz
Total Bandwidth Swept	B	7 MHz
Delay Time Resolution	Δt	125 ns

- Real world measurements are taken between 25 m – 425 m TX–RX separation with the same altitude at 50 m.

- Number of measurement locations is 21 and each point includes four data sets to take the average, as given in Figure 5.1(b).

- Location and timestamp of each measurement point are also saved at Raspberry Pi 4 which help obtain the exact location of the Tx–Rx via UAVs GPS data.

- To protect the hardware of the measurement equipment, RF power amplifiers are not used while taking the measurements at the anechoic chamber, which leads to linear received power offset between two measurements settings of Figure 5.6.

- **Sweeping:** The transmitter sends a sweeping chirp signal continuously between 5.820 45 GHz and 5.827 55 GHz with 50 kHz step size. Sweeping between frequencies has 1.448 millisecond duration.

- **Interference:** Before the measurements, RF spectrum is monitored with a Rohde&Schwarz FSW26R spectrum analyzer in order to ensure that there is no interference within the measurement frequency of 5.820 45 GHz and 5.827 55 GHz. It is seen that the remote controller of UAVs uses frequency band up to 5.82 GHz. Thus, we select 5.820 45 GHz and 5.827 55 GHz to avoid contamination.

- **I/Q Record:** During the measurement, Raspberry Pi 4 controls the bladeRF by using a bash script to receive the signal when UAV reaches the next point on the grid. At each measurement point, the script on Raspberry Pi 4 runs on an Android device, and 8 MHz bandwidth measurements with a central frequency of 5.824 GHz are taken for 1 second.

- **Raspberry buffer size:** The reason for choosing 16 MS/s sample rate is the constraints of Raspberry Pi 4 buffer size in terms of I/Q saving on a file.

- **ADC digital filter:** It is observed that receiver SDR's ADC digital filter has the side effect that actual bandwidth is less than desired bandwidth, so actual bandwidth is selected as 8 MHz bandwidth although desired bandwidth is 7 MHz.

- **DC offset:** Furthermore, in order to eliminate the effect of DC offset in the receiver, the center frequency is selected as 5.824 GHz and that frequency intentionally left blank in the transmitter. Measurement parameters are listed in Table 3.1.

The captured data is saved on the Raspberry Pi 4. Furthermore, data is fed into a desktop computer running Matlab to analyze the captured received signals.

4. MEASUREMENT BASED STATISTICAL CHANNEL ANALYSIS OF AIR–TO–GROUND PATH LOSS MODEL IN LOW ALTITUDE UAVS

Despite all of the measurement campaigns, results, and theoretical analyses present in the literature which are mostly focused on 800 MHz–850 MHz, 960 MHz–977 MHz and 5030 MHz–5091 MHz for the UAV communication, a generic and comprehensive propagation model for emergency case communications focusing specifically on UAVs operating at UHF bands is still required. Therefore, in this chapter, a single–frequency path loss measurement campaign at 446 MHz is proposed. Air–to–ground link is established via a channel sounder system mounted on UAV. Measurements are collected within a suburb district, which is located close by to an inner sea. Measurement site is of hilly terrain structure with foliage. Considering the fact that such topographical layouts are difficult to reach and collect measurement data, this section paves the way for incorporating various terrain profiles into the channel models and obtaining a more comprehensive air–to–ground propagation link.

4.1 General Large Scale Characteristics of Air–to–Ground Link for UAV

In a general air–to–ground wireless communication link scenario, it is frequently reported in the literature that the propagation mechanism at large scale is governed by the following statistical path loss equation:

The general equation for a path loss model that includes both shadowing and fading on a dB scale is typically expressed as:

$$PL(d) = \underbrace{20 \times \log \frac{4\pi d_0}{\lambda}}_{PL_0} + 10\eta \log_{10}\left(\frac{d}{d_0}\right) + X_\sigma \qquad \textbf{(4.1)}$$

Here, $PL(d)$ represents the average path loss at distance d, and $PL(d_0)$ represents the reference path loss at a reference distance d_0. The value of η represents the path loss exponent, which is dependent on the environment. X_σ represents the shadowing loss. X_σ is typically modeled for Air–to–Ground systems as random variable with Gaussian distribution. Shadowing loss occurs due to phase shifts of signals arriving via multiple

4.3(a).

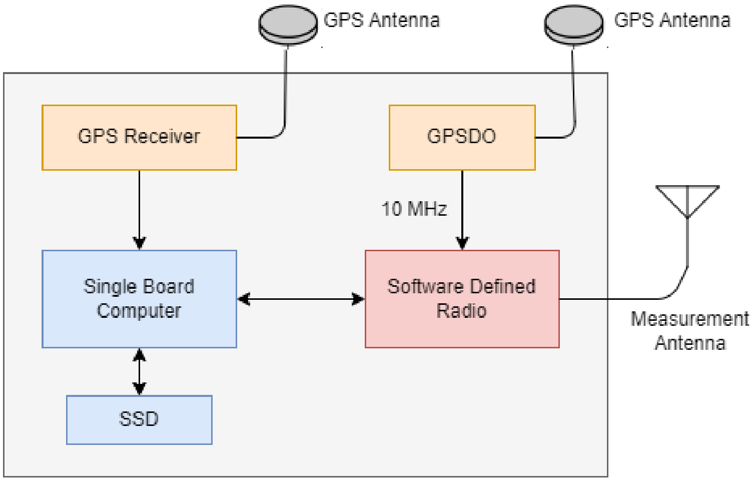

Figure 4.1 : Transceiver system schema.

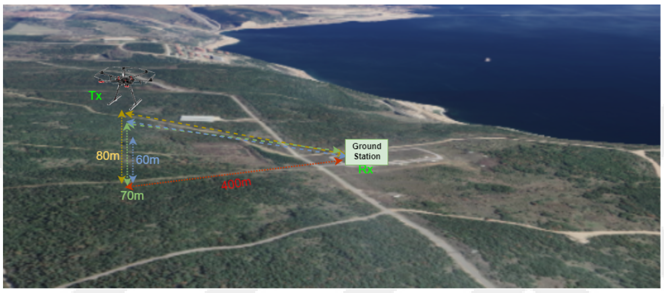

Figure 4.2 : Block diagram for measurement setup.

paths and is a slow process. Note that all losses (path loss exponent, shadowing loss) are expressed in dB.

4.2 Measurement Campaign

4.2.1 Measurement setup

The measurements are collected in the test field at the Scientific and Technological Research Council of Turkey (TUBITAK) in Gebze, as illustrated in Figure 4.2. This field provides a realistic scenario for studying wireless communication systems and their performance in a real-world environment. A channel sounder signal is used to transmit a PN sequence with 4095 length in 446 MHz center frequency on the UAV side. DJI Matris 600 Pro is flown up to obtain measurements and it is used as an air station for its payload capability and durability in extreme conditions. It is shown in 4.3(a).

On the other hand, the same system on the transmitter in 4.3(b) in the car, is used as a ground station to receive the transmitting signals. Signals have 50MHz bandwidth and

(a) Transmitter system on UAV. (b) Receiver system on ground station

Figure 4.3 : Transceiver system for real.

50ns time resolution. Furthermore, a monopole antenna which a frequency ranging from 400MHz to 470MHz is used for the ground station to receive the transmitted signals. The antenna has an omnidirectional radiation pattern and it has a 3.3 dBi antenna gain at 433MHz. After the calculation of the received powers of each point, the path loss model is extracted as it will be explained in Section 4.3.

4.2.2 Measurement methodology

To begin with the transmitter side, the software-defined radio (SDR) is configured by the single-board computer (SBC). The carrier frequency and bandwidth are set to 446 MHz and 50 MHz, respectively, and a predefined pseudo-random noise (PN) sequence of length 4095 is continuously generated by the SBC from the solid-state drive (SSD) to support a data transmission rate of 1.6 Gbps. The SDR processes the IQ data and converts it to radio frequency (RF) signals, which are amplified up to 30 dBm before being transmitted via the antenna.

On the receiver side, the SDR is configured with the same parameters as the transmitter, including the carrier frequency and bandwidth, before starting the measurement recording. The antenna collects the over-the-air signals, which are then processed by the SDR to convert the RF signals into IQ data. The SBC stores the IQ data, consisting of 81900 samples, periodically to the SSD every 100 ms. Both the transmitting and receiving SDRs are precisely synchronized with a 10 MHz clock from the Global Positioning System Disciplined Oscillator (GPSDO), and the GPS receiver provides high-precision location measurements for both drone and ground station. To ensure consistency in post-processing analysis, the measurements are recorded by combining the locations of the measurement points for the same scenario. The measurements are collected from 60m to 80m heights with step sizes 10m vertically. Local regulations allow UAV to operate up to 120m in height, however, due to the topographical conditions and the high wind speed after 80m in height, measurements are performed for 60m to 80m in height. Moreover, the only allocated location for UAV flight, where the measurement is taken, is shown in Figure 4.3(b) in TUBITAK, Gebze. Also, for each vertical measurement point, UAV moves between 10m to 410m horizontally.

In this air-to-ground channel measurement system, a PN-sequence based channel sounder with a 50 MHz bandwidth is utilized for the purpose of path loss calculations. The system is capable of accurately determining the path loss in the 50 MHz band, which is a crucial parameter in the design of wireless communication systems. Path loss measurements are performed using a variety of techniques, including signal strength measurements, distance measurements, and modeling approaches. In this particular system, the PN-sequence based channel sounder provides a direct method of measuring path loss by transmitting a known signal and measuring the received signal strength. The results of the path loss measurements are then analyzed to determine the optimal signal strength and frequency range for wireless communication in the 50 MHz band. Overall, this system provides a valuable tool for evaluating the performance of wireless communication systems in the 50 MHz band, and can help to optimize their design and implementation.

4.3 Measurement Results

The measurement campaign focuses on the relationship between the received power of a narrowband signal and the distance between the transmitter and receiver (Tx–Rx separation), taking into account both horizontal and vertical distance. This relationship is illustrated in Figure 4.4, which shows that the received power decreases with increasing Tx–Rx separation, as expected. In Figure 4.4, the measurement results are given together with the figures of the free space path loss and the path loss log-distance model obtained as a result of least-squares estimation. Using least-squares estimation on the measurement data, we can derive the following path loss models:

$$\mathrm{PL(dB)} = \begin{cases} 2.0516 \times d + 25.23, \ a = 60m \\ 1.9119 \times d + 28.15, \ a = 70m \\ 1.9554 \times d + 27.15, \ a = 80m \end{cases} \tag{4.2}$$

where d is the transmitter–receiver separation and a stands for the altitude of UAV.

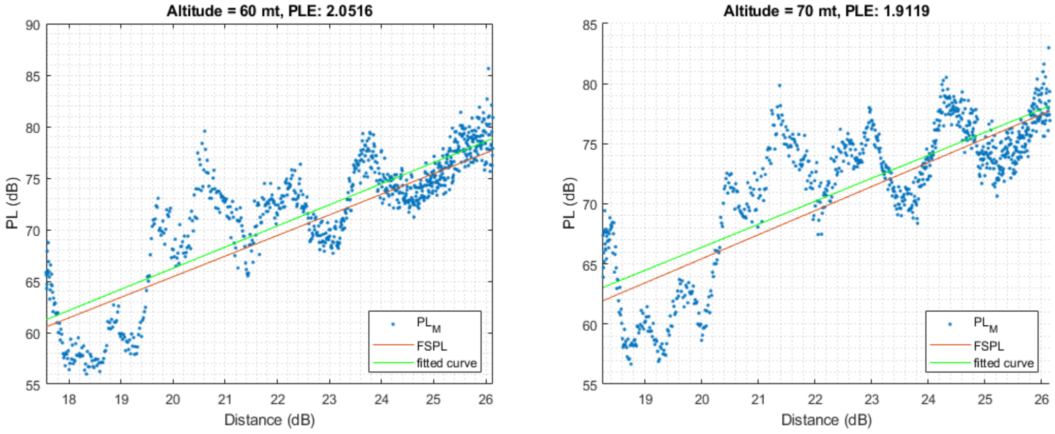

(a) 60m altitude.

(b) 70m altitude.

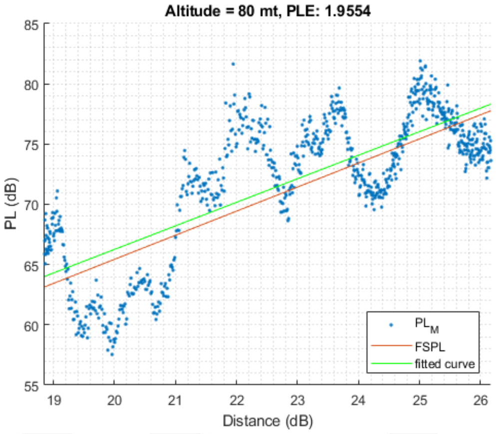

(c) 80m altitude.

Figure 4.4 : Measurement results for path loss at different altitudes.

For the sake of brevity, the path loss coefficients for specific frequencies and altitudes are listed in Table 4.1. Overall mean path loss exponent is found to be $\eta = 2.0516, 1.9119, 1.9554$ for the altitudes of 60 m, 70 m, and 80 m, respectively. Another important observation, which is also in conformity with the results presented in the literature in different frequencies [2]. Furthermore, the shadowing results are given in Figure 4.5, 4.6, 4.7 to explain the possible reason for the path loss fluctuates.

It shows the residual value when the log-distance path loss value is subtracted from the shadowing effect path loss expression expressed in Equation 4.1. In Figure 4.5(a), the shadowing effect was obtained for 60m altitude, and when the CDFs of the experimental results and the reference signal with $\sigma = 3.1947$ dB standard deviation were compared to the zero-mean Gaussian distribution, it was observed that it fit into the zero-mean Gaussian distribution as shown in Figure 4.5(b).

For the case of 70m altitude, the residual value can be obtained by subtracting the log-distance path loss value from the shadowing effect path loss expression expressed

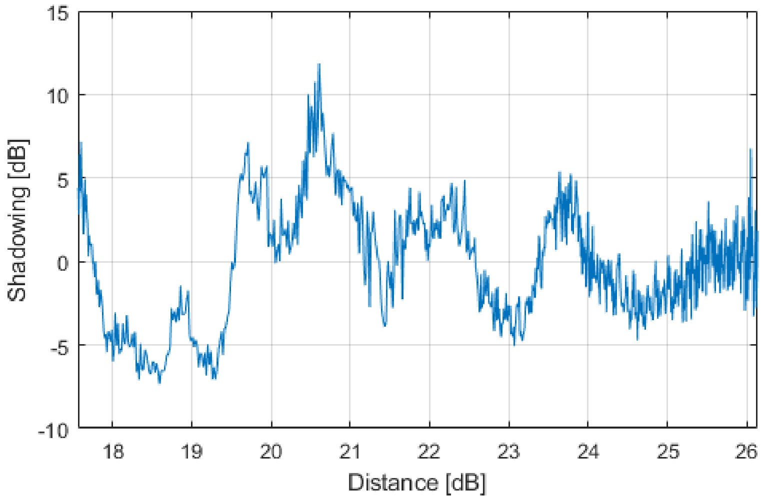

a: σ=3.1947dB

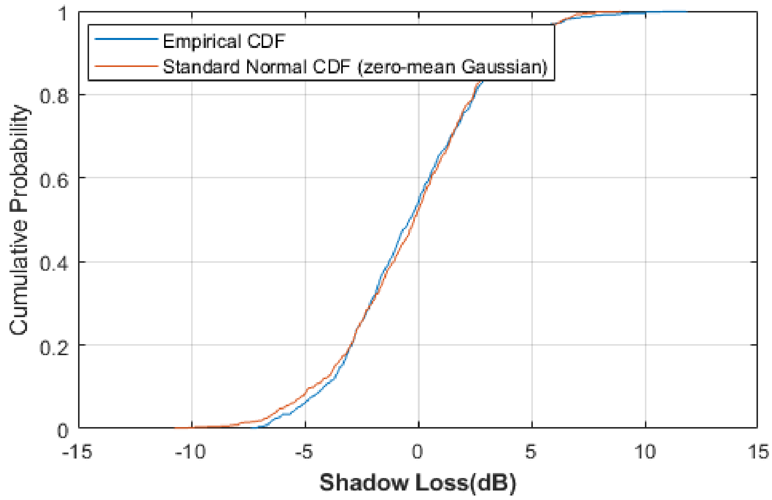

b: CDF

Figure 4.5 : Measurement results for shadowing at 60 m altitude.

in Equation 4.1. Figure 4.6(a) shows the resulting shadowing effect, and the CDFs of the experimental results and the reference signal with $\sigma = 3.4566$ dB standard deviation were compared to the zero-mean Gaussian distribution and were found to closely follow the distribution, as depicted in Figure 4.6(b).

Similarly, for the case of 80m altitude, the residual value can be obtained by subtracting the log-distance path loss value from the shadowing effect path loss expression expressed in Equation 4.1. Figure 4.7(a) shows the resulting shadowing effect, and when the CDF of the obtained shadowing signal was examined, it was observed that the CDFs of the experimental results and the reference signal with $\sigma = 3.632$ dB standard

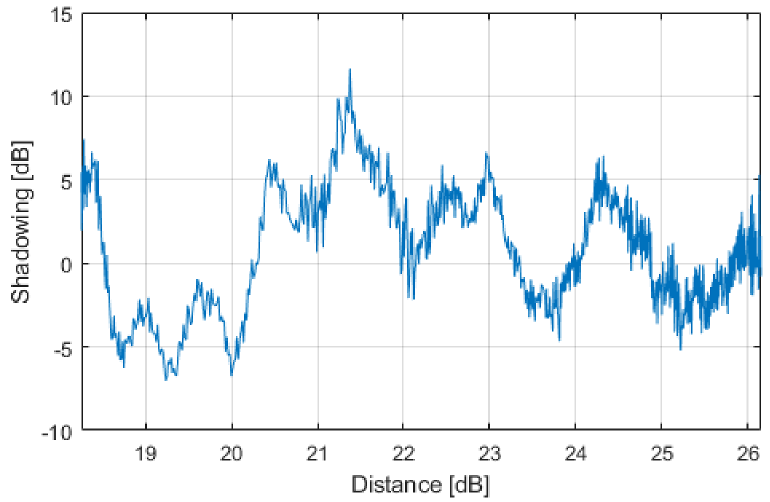

a: σ=3.4566dB

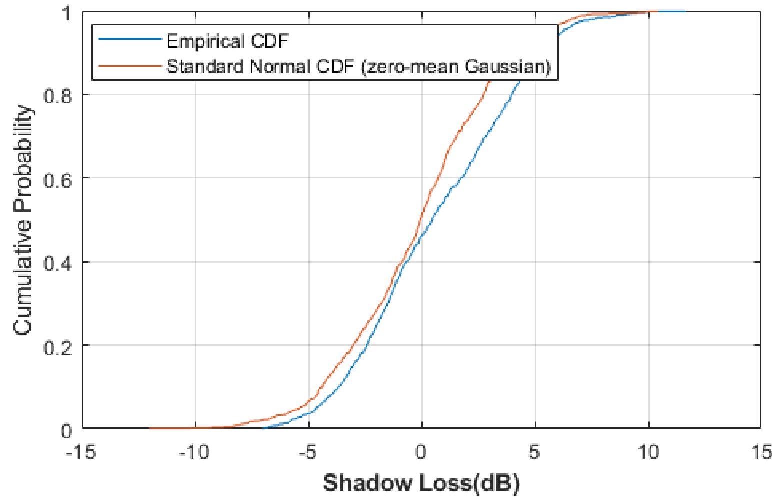

b: CDF

Figure 4.6 : Measurement results for shadowing at 70 m altitude.

deviation were compared to the zero-mean Gaussian distribution, as shown in Figure 4.7(b).

The shadowing results in such topology illustrated in Figure 4.3(b) are expected because there are many trees and a few buildings with metal structures in the measurement environment. It is worth emphasizing the significance of the standard deviation values associated with log-normal shadowing, as they demonstrate excellent agreement with the values reported in the existing literature [43]. Specifically, within the range of 3 dB to 5 dB, our findings align closely with the documented values. This concurrence reinforces the validity and reliability of our measurements, validating the consistency and accuracy of our research methodology.

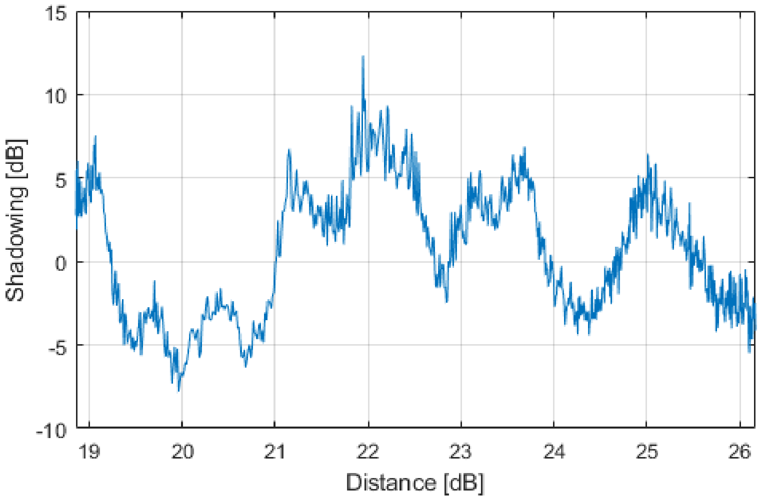

a: σ=3.632dB

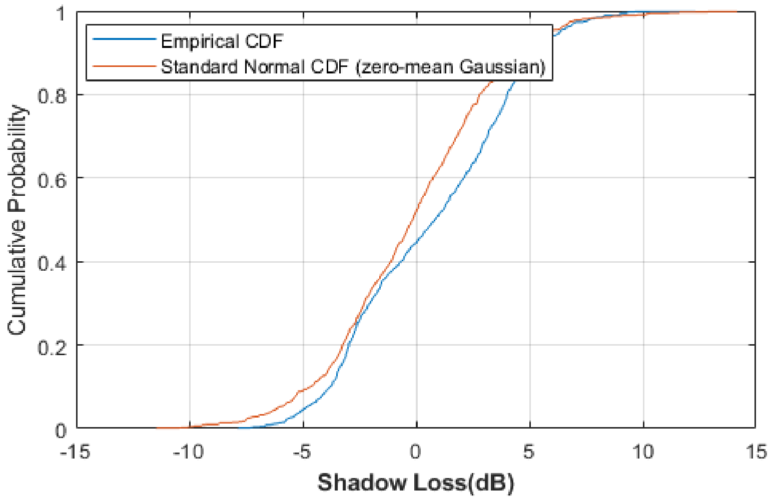

b: CDF

Figure 4.7 : Measurement results for shadowing at 80 m altitude.

Table 4.1 : Values for $D_{\max}$ and Path Loss Exponent, η and Shadowing for 446 MHz at different altitudes.

Altitude (m)	60	70	80
PL. Exp. (η)	2.052	1.912	1.955
Shadowing σ (dB)	3.195	3.457	3.632

4.4 Summary

In this work, the results of a measurement campaign for air-to-ground channels of UAV at 446 MHz are presented due to the fact that refarming of UHF band will enable new opportunities for emergency case situations. The path loss models for specific altitudes were derived using least-squares estimation on the measurement data. The shadowing results were given for different altitudes, and it was observed that the CDFs of the experimental results closely follow the zero-mean Gaussian distribution. These results are expected due to the many trees and few buildings with metal structures in the measurement environment. The standard deviation values of log-normal shadowing are compatible with the values reported in the literature. Finally, in future studies, we will extend our results to multiple frequency ranges by also incorporating environmental effects in different locations and topographies.

5. AIR–TO–AIR CHANNEL MEASUREMENTS AND MODELING IN RURAL ENVIRONMENTS FOR LOW ALTITUDE UAVS

In this section, a channel measurement system is developed for UAVs at 5.8 GHz. BladeRF 2.0 micro xA9 SDR based channel sounder is employed to capture over the air transmission. Although over the air UAV communication exhibit many fundamental propagation behaviors, LOS state should be the first analyzed due to the fact that LOS provides the basic yet not well–established characteristics. To accurately model the wireless channel, it is important to first conduct a thorough investigation of the LOS measurements. This will provide a solid foundation for developing a systematic and comprehensive statistical channel model. In this section, we present detailed discussions of the measurement setup and provide large-scale channel propagation statistics, such as the path loss exponent, to support our analysis. Comparison of results which encompasses several other methods for path–loss modeling is also provided.

The 5.8 GHz frequency band is a highly suitable option for UAV communication due to its high data rate, low atmospheric attenuation, and unlicensed usage. In order to optimize and analyze the communication channel characteristics between UAVs, it is important to perform measurements at the 5.8 GHz band. These measurements allow for the analysis of critical parameters such as path gain, Doppler spectrum, and time-frequency correlation function. Additionally, measuring at the 5.8 GHz band is necessary to evaluate the impact of UAV mobility and trajectory on the communication channel. In particular, scenarios involving UAVs with varying speeds and directions in both horizontal and vertical planes require non-stationary channel assumptions. Finally, measuring at the 5.8 GHz band is beneficial for developing a realistic and efficient UAV channel model. This model can be used to simulate and improve the performance of UAV communication systems, ultimately leading to more effective and reliable UAV operations [24], [44].

5.1 Transmitted Signal and Analysis Methods

Driven by the measurement scenario, campaign, and relevant constraints, transmit signal is constructed as a windowed stepped frequency sweep:

$$x(t)=\sum_{k=1}^{K}e^{j(2\pi f_k t+\varphi_k)}w_k\left(t-B_k\right) \tag{5.1}$$

where K is the total number of bursts to be swept; $w_k(t)$ denotes the windowing function which is operational for $t\in[0,T]$ where T is the observation time; B_k stands for the sum of all time gaps and burst durations up to kth burst; f_k and φ_k represent the carrier frequency and initial phase of the kth burst, respectively. For the sake of ease in representations, let frequencies to be swept be given as a set where $f_k\in\{f_1,f_2,f_3,\cdots,f_p\}$ where p denotes the total number of available frequencies. Without loss of generality, the windowing function could be considered to be a rectangular function given as:

$$w_k(t)=\left\{\begin{array}{ll}1, & t\in[(k-1)T_h,kT_h)\\ 0, & \text{others}\end{array}\right. \tag{5.2}$$

where T_h is the burst duration. Considering the time-invariant system, the generalized channel model can be represented as,

$$h(t)=\sum_{i=1}^{L}a_i\delta(t-t_i) \tag{5.3}$$

where L denotes the number of paths, a_i stands for the channel coefficient of the ith multi–path, and t_i represents the propagation delay of the ith multi–path. The received signal can be written as,

$$r(t)=h(t)*x(t)+n(t) \tag{5.4}$$

where $*$ is the convolution operator and $n(t)$ stands for the complex additive white Gaussian noise (AWGN) in this case, the I and Q components are independent and identically distributed (i.i.d.) random variables with a normal distribution having mean 0 and variance $\sigma^2/2$.

5.1.1 Time analysis

The power calculation of the received signal with the time analysis method is the classical power calculation method depending on the time samples of the received signal without any post–processing. The average power can be achieved by averaging the instantaneous powers of the $r(t)$ and can be calculated as,

$$P_{r,d} = \frac{1}{T}\int_0^T |r_d(t)|^2\, dt \tag{5.5}$$

where $r_d(t)$ is the equivalent received signal for dth distance. Among the wireless impairments, there are such physical effects as the randomness of the drone movements and of the weather conditions that might cause fluctuations in the power of the received signal. These effects are averaged-out by taking several measurements for each distance as,

$$E\{P_{r,d}\} = \frac{1}{M}\sum_{m=1}^{M} P_{r,d,m} \tag{5.6}$$

where $E\{\cdot\}$ is the spatial averaging operator and M denotes the number of measurements for each distance.

5.1.2 Frequency analysis

Considering the frequency domain properties, the signal power concentrates on each center frequency of the swept signal. Defining the $R(f)$ is the Fourier Transform of the $r(t)$, power of the received signal in frequency domain can be calculated as,

$$P_R = \sum_{i=1}^{p} |R(f_i)|^2 \tag{5.7}$$

where i represents the center frequencies of the swept signal. Note that averaging process is included to achieve $R(f)$ from $r(t)$. Therefore, only sum operation is used to calculate the power. Additionally, spatial averaging is considered for power calculation.

5.1.3 A novel perspective of time–frequency Analysis

Because of the wireless impairments that affect the received signal, the statistical characteristics of the signal might change. Ensemble averaging can be used to suppress these impairments so that the statistical characteristics of the signal can be preserved. To overcome this issue, it is necessary to extract each burst from the wideband spectrum and estimate the parameters of the sweep signal. One way to accomplish this is by using time–frequency analysis, such as short time Fourier transform (STFT), to estimate several temporal parameters, such as the duration and start/stop time of each burst, as well as the center frequency of the signal. The STFT is computed by applying a time–varying window to the captured signal and then taking the discrete Fourier transform (DFT) of the windowed signal. This allows for accurate estimation of the temporal and frequency characteristics of the bursts in the wideband spectrum [45,46]. Since the received signal contains more than one period of the signal waveform during the observation time, the bursts having the same center frequencies are clustered into same classes. Then, each of these bursts in the same class is extracted from the received signal for a specified time interval, or time window. After extracting each burst, the ones with the same center frequencies sum up to achieve the ensemble average of the signal. Imperfections in the estimation of the parameters that occur in the burst extraction process yield differences in transition effects. Ensemble averaging also eliminates these effects. Let $\hat{z}_i(t)$ be the averaged version of ith frequency channel and can be represented as,

$$\hat{z}_i(t) = \frac{1}{N}\sum_{j=0}^{N-1} r(t + B_{i+pj}) \times g(t) \tag{5.8}$$

where $r(t)$ is the received signal, N represents the number of bursts that occur in ith channel frequency during the observation time, and $g(t) = u(t) - u(t - \hat{T}_h)$ where $u(t)$ is step function and $\hat{T}_h$ denotes the estimated duration of the burst.

To improve the resolution of the signal, it is necessary to remove the gaps in time between hops. To do this, we can define a concatenated function, $\hat{f}(t)$, which combines or "stitches" together the individual hops to create a continuous signal. This allows for more accurate estimation of the temporal and frequency characteristics of the signal,

$$\hat{f}(t) = \sum_{i=1}^{p} \hat{z}_i(t - (i-1)T_h). \tag{5.9}$$

By combining Equations **(5.8)** and **(5.9)**, the overall reconstruction process from $r(t)$ to $\hat{f}(t)$ can be expressed as:

$$\hat{f}(t) = \frac{1}{N}\sum_{i=1}^{p}\sum_{j=0}^{N-1} r\left(t - (i-1)T_h + B_{i+pj}\right) \times g(t - (i-1)T_h) \tag{5.10}$$

and the average power of the ensemble–averaged signal is calculated,

$$P_{\hat{f}} = \frac{1}{T_f}\int_0^{T_f} \left|\hat{f}(t)\right|^2 dt \tag{5.11}$$

where T_f is the sum of the bursts duration. Note that, spatial averaging is considered for power calculation.

5.1.4 Large scale characteristics

Large scale characteristics for A2A wireless communication link can be described by the following path loss equation:

$$\Lambda(d) = \underbrace{20 \times \log \frac{4\pi d_0}{\lambda}}_{PL_0} + 10\eta \log (d/d_0) + \zeta_{LOS}, \tag{5.12}$$

In the equation above, d represents the distance between the transmitter and receiver. This distance is a key factor in determining the received power of the signal, as it directly affects the path loss, η denotes the path loss coefficient which depends on the environment, d_0 stands for the reference distance for path loss measurements, and PL_0 represents the free–space path loss, and ζ_{LOS} contains all of the large–scale characteristic losses for LOS.

5.2 Measurement Setup

5.2.1 Measurement environment

To verify antenna pattern and free space path loss performance, a measurement setup is constructed in the Antenna Test and Research Laboratory (ATAM) of TUBITAK BILGEM as shown in Figure 5.1(a). The dimensions of the anechoic chamber is 17 m × 18 m× 14 m (L×W×H) and frequency range is 0.5 GHz – 40 GHz. Field measurements are taken at the TUBITAK BILGEM Gebze campus (as shown in Figure 5.1(b)) which consists of a rural area with trees causing ground reflection signal to drastically lose its power, hence the reflected signal power falls below the noise level. The location of the stationary receiver and the route followed by the transmitter during the measurement on a 3D map are also exhibited in Figure 5.1(b).

5.2.2 Measurement equipment

As shown in Figure 5.2, two identical DJI Matrice 600 Pro hexacopter drones are used as receiver and transmitter. The channel measurement box contains the TX and RX modules are attached to drones. Each TX and RX channel measurement box consist of

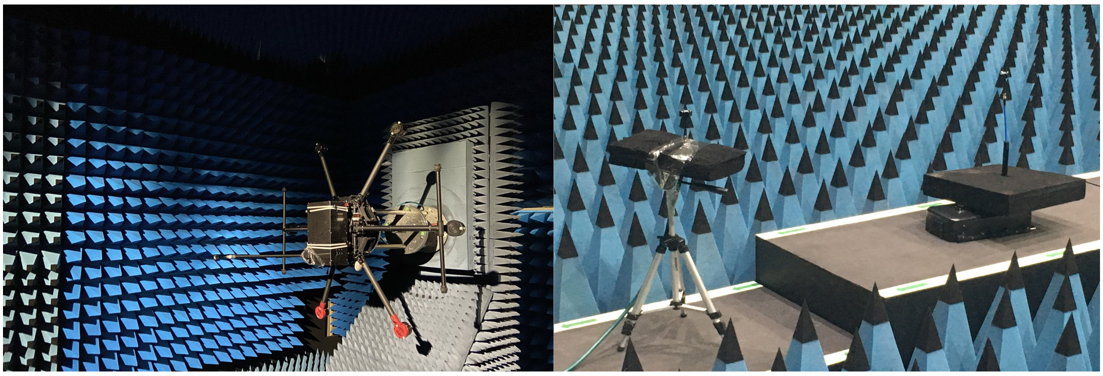

(a) Anechoic chamber measurements for analysing the coupling effect (left). Guaranteeing the free space LOS conditions by using an anechoic chamber for isolation (right).

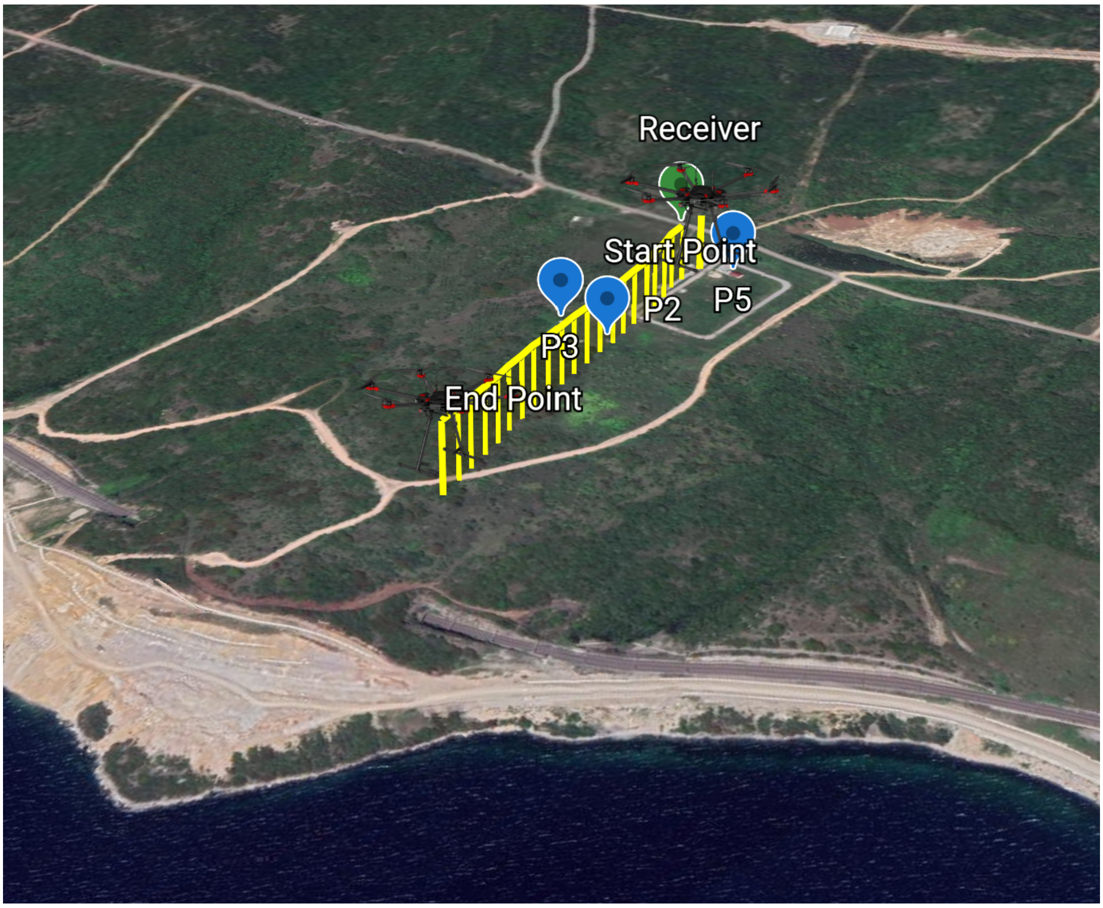

(b) The location of the stationary receiver and the route followed by the transmitter during the measurement on a 3D map.

Figure 5.1 : Two perspectives of the measurement campaign.

one bladeRF 2.0 micro xA9 transceiver, a Lucix S020180L3205 RF power amplifier to boost signal for both side, as a mini computer Raspberry Pi 4B, CP antenna and 28 600 mA h powerbank which has high current capability is used as battery. Antenna radiation pattern is shown in Figure 5.3. The coupling effect of the drone on the radiation pattern of the antenna is analyzed, and in this regard, the measurements

Figure 5.2 : Illustration of the measurement campaign in which two commercially available hexacopter are used as transmitter and receiver. Note that two drones are ready to take–off with mounted channel measurement box.

are taken under the presence and absence of the drone at the anechoic chamber. It can be seen that the coupling effect of the drone can be considered negligible level as shown in Figure 5.3(a) and Figure 5.3(b) for elevation and azimuth directions, respectively. Furthermore, to facilitate seamless control of both the Raspberry Pi 4 units from the ground, an Android cellular phone serves as a central control device. This Android phone effectively acts as a remote controller, enabling convenient management and coordination of the Raspberry Pi 4 devices. The comprehensive measurement system employed in the experiment is illustrated in Figure 5.4, providing a visual representation of the system's architecture and components. Additionally, Figure 5.5 showcases the dedicated channel sounding equipment utilized in the study. It is important to highlight that a back-to-back calibration approach is implemented, incorporating RF cable connections. This calibration methodology compensates for any potential impairments introduced by the aforementioned devices, ensuring accurate and reliable measurement results. By employing this meticulous calibration technique, the measurement system achieves enhanced performance and mitigates the impact of inherent device-related imperfections, further bolstering the credibility and precision of the experimental measurements.

5.2.3 Measurement methodology

Measurement campaign is performed as two–folds as anechoic chamber and real world measurements. (a) Anechoic chamber measurements are taken for separation distances of 1 m, 2 m, 3 m and 4 m, respectively as seen in Figure 5.1(a) and (b) real world measurements are taken between 25 m–425 m TX–RX separation with the same

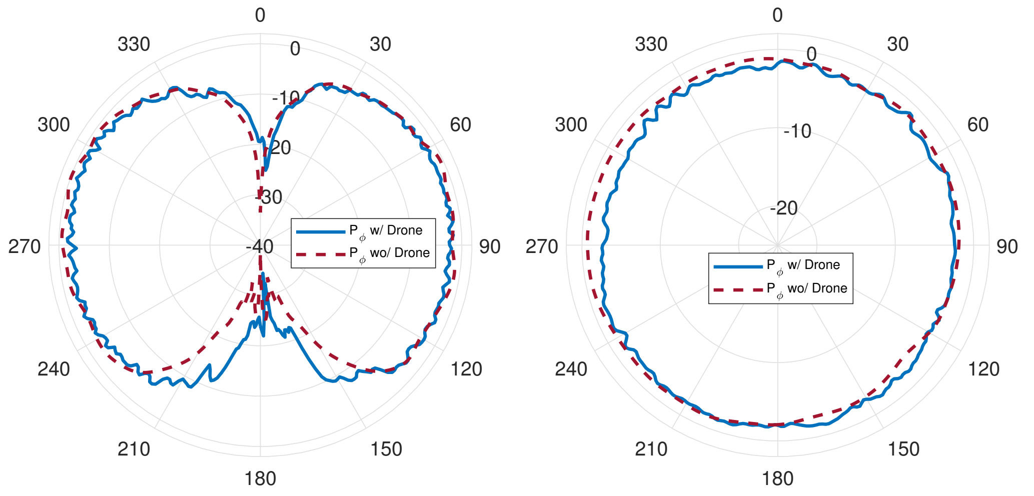

(a) Elevation radiation pattern planes for the CP antenna.

(b) Azimuth radiation pattern planes for the CP antenna.

Figure 5.3 : The result of the antenna pattern measurement for both presence and absence of the drone.

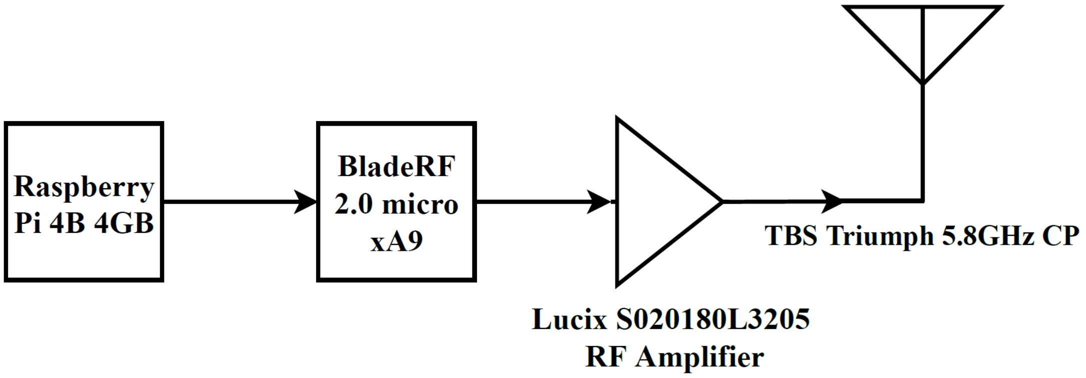

Figure 5.4 : The block diagram of channel sounder for both transmitter and receiver (arrows are in the reverse direction) used in measurement campaign and equipment.

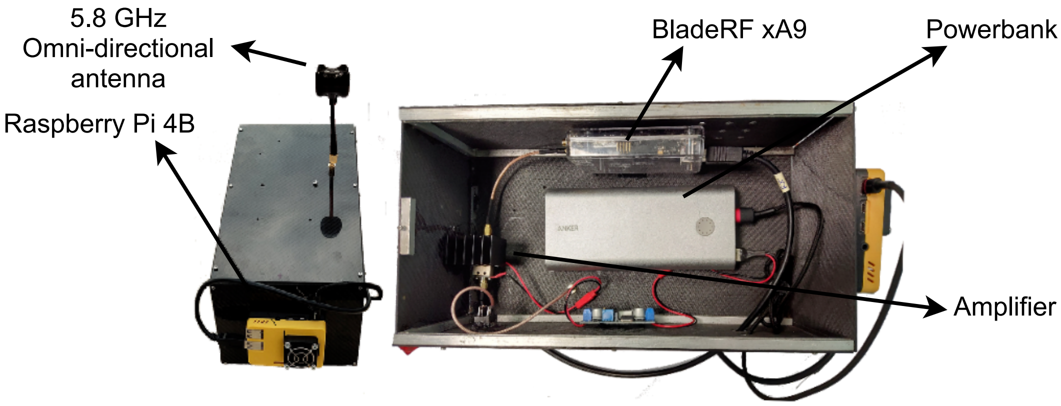

Figure 5.5 : Actual picture of the channel measurement box operating at 5.8 GHz.

altitude at 50 m. Number of measurement locations is 21 and each point includes four data set to take average, as given in Figure 5.1(b). Location and timestamp of each measurement point are also saved at Raspberry Pi 4 which help obtain exact location of the Tx–Rx via UAVs GPS data. To protect the hardware of the measurement equipment, RF power amplifiers are not used while taking the measurements at the anechoic chamber, which leads to linear received power offset between two measurement settings of Figure 5.6 and Figure 5.7.

The transmitter sends a sweeping chirp signal continuously between 5.820 45 GHz and 5.827 55 GHz with 50 kHz step size. Sweeping between frequencies has 1.448 millisecond duration. Before the measurements, RF spectrum is monitored with a Rohde&Schwarz FSW26R spectrum analyzer in order to ensure that there is no interference within the measurement frequency of 5.820 45 GHz and 5.827 55 GHz. It is seen that the remote controller of UAVs uses frequency band up to 5.82 GHz. Thus, we select 5.820 45 GHz and 5.827 55 GHz to avoid contamination. During the measurement, Raspberry Pi 4 controls the bladeRF by using a bash script to receive signal when UAV reach next point on the grid. At each measurement point, the script on Raspberry Pi 4 run on Android device and 8 MHz bandwidth measurements with a central frequency of 5.824 GHz are taken during 1 second. The reason for choosing 16 MS/s sample rate is constraints of Raspberry Pi 4 buffer size in terms of I/Q saving on a file. It is observed that receiver SDR's ADC digital filter has side effect that actual bandwidth is less than desired bandwidth, so actual bandwidth is selected as 8 MHz bandwidth although desired bandwidth is 7 MHz. Furthermore, in order to eliminate the effect of DC offset in the receiver, center frequency is selected as 5.824 GHz and that frequency intentionally left blank in the transmitter. Measurement parameters are listed in Table 3.1.

The captured data is saved on the Raspberry Pi 4. Furthermore, data is fed into a desktop computer running Matlab to analyze the captured received signals.

5.3 Measurement Results

In this section, measurement results are analysed first starting with anechoic chamber results. Figure 5.6 shows the signal powers versus log-distance for time–based method, time–frequency method, and frequency method. According to received signal powers, the least-squares estimation is utilized to estimate the PLE and signal power offset. The

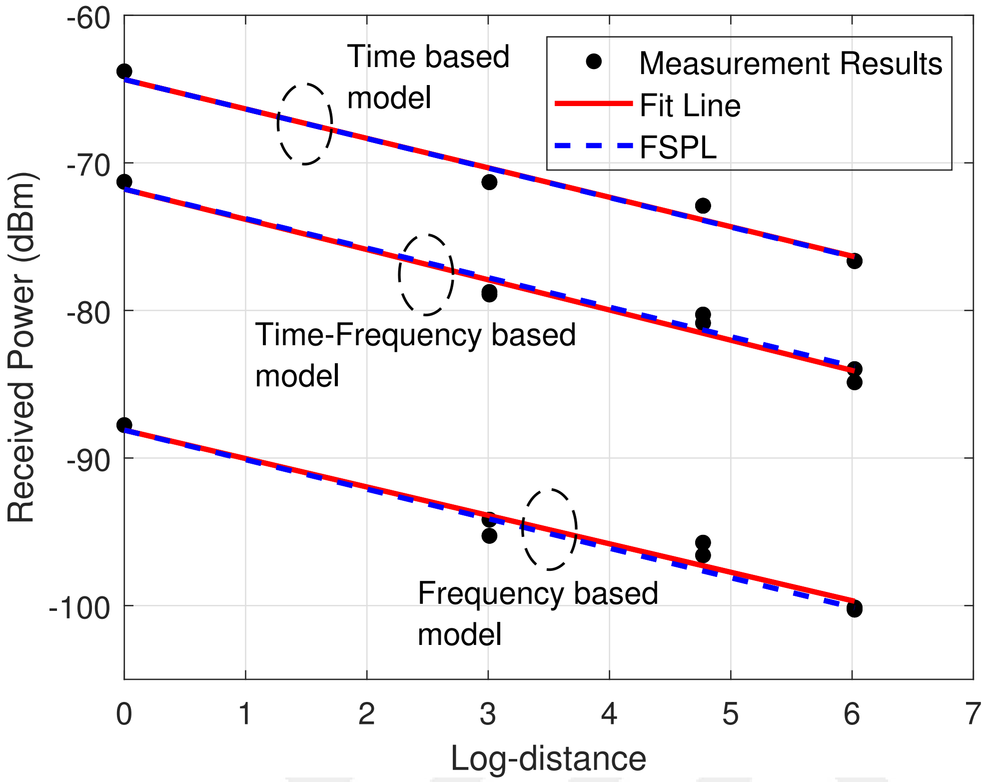

Figure 5.6 : PLE, η, comparison for the anechoic chamber measurements and FSPL exponent for time, time–frequency, and frequency methods, respectively. Due to not using RF power amplifiers, the initial power value is lower. Log–distances are calculated through $10 \times \log_{10}(d)$ where d is in meter.

results demonstrate that PLE can be estimated by time–based method, time–frequency method, and frequency method as 1.995, 2.046, and 1.932, respectively. Therefore, these methods are thought to be utilized trustfully for A2A measurements. Recalling that the frequency method only uses the peak power of each center frequency, signal power offset for the frequency–based method is appeared lower. Time– frequency based power estimation model aims to avoid the time transition anomalies whereas the time based model calculates the average of the entire STFT matrix. Since the aforementioned models focus on the different portions of time-frequency data, the power averages calculated by the models tend to variate from each other. Once we have verified that the proposed method can accurately estimate the PLE of the A2A communication system, we can post-process the raw time data to estimate the PLE of the system. This is accomplished by applying various algorithms and techniques to the data to extract the necessary information and improve the accuracy of the results. The received signal powers are calculated for each distance and each method at 5.8 GHz.

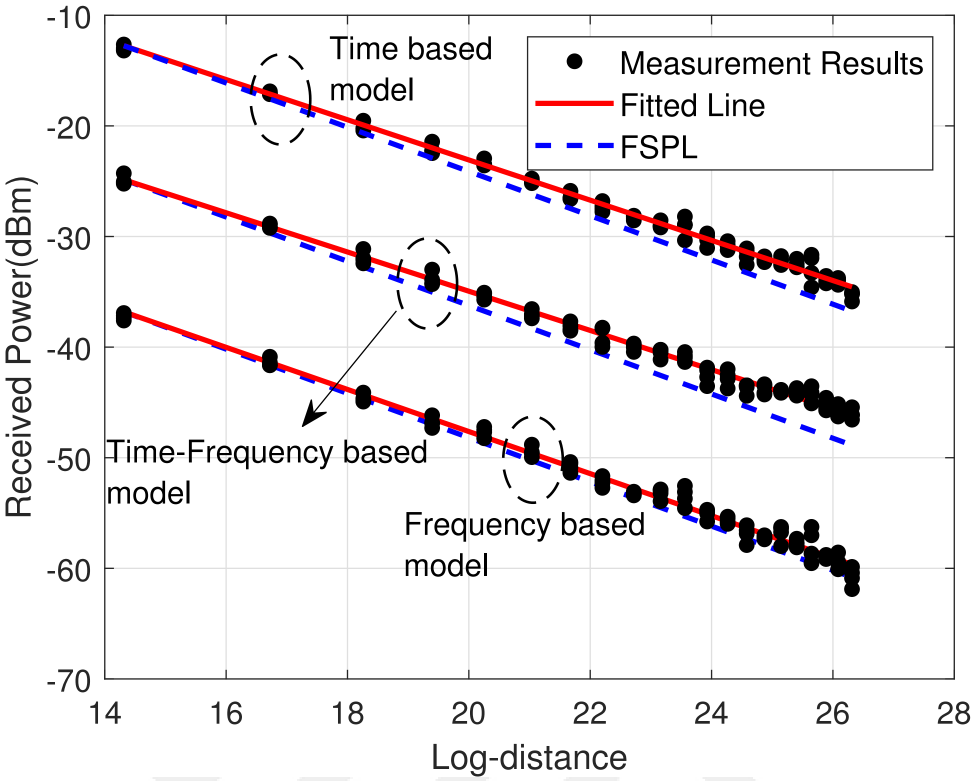

Figure 5.7 : PLE, η, comparison for the real world A2A measurement results and free space path loss exponent for time, time–frequency, and frequency methods, respectively. Due to using RF power amplifiers, the initial power value is higher. Log–distances are calculated through $10 \times \log_{10}(d)$ where d is in meter.

Subsequently, all 84 measurement points are used to fit a line in log–log graph. Results of this procedure for each method are given in Figure 5.7. A2A path loss model is estimated as,

$$PL(dB) = \begin{cases} 1.817 \times 10\log_{10}(d) + 6.74, & \text{Time} \\ 1.773 \times 10\log_{10}(d) + 19.4862, & \text{Time–Freq.} \\ 1.903 \times 10\log_{10}(d) + 29.573, & \text{Frequency} \end{cases} \quad \textbf{(5.13)}$$

In the equation above, d represents the distance between the transmitter and receiver. Besides, d_0 is selected 28 m for this scenario. The RMSE values of fitting for the time based, time–frequency based, and frequency based are respectively 0.5161, 0.5388, and 0.6885. These measurement results also comply with the analytical works of [2] and [47], thus provides a solid foundation for A2A channel characteristics. Note that the reason behind the difference between the power levels of Figure 5.6 and Figure 5.7 is that RF power amplifiers are used in the A2A measurements.

6. CONCLUSION AND FUTURE DIRECTIONS

From the USRP used in the UAV channel modeling measurement system to the mobile transceiver design; from the used amplifier to the Raspberry Pi; problems have been encountered in a variety of areas, ranging from the GPS module to remote measurement software, and suitable solutions have been suggested. Center frequency shift, DC leakage, and I/Q imbalance were observed in USRPs, respectively, frequency shift correction in the receiver after frequency shift cross-section, design of filters specific to DC leakage, matrix-based imbalance estimation and correction in I/Q imbalance or second order I/Q. Based on the statistics, solutions such as correction have been proposed. In addition, the issues that need to be considered in the amplifiers used in creating a mobile measurement system, the selection of power supply with the appropriate DC-DC converter, how the Raspberry Pi 4B is used for remote control and how the GPS module is used to track the location of the receiver and transmitter. Finally, in the algorithm section, the statements about how the described devices will interact with one another, the channel model system will be used, how to link remotely, and how the measurement will be managed parametrically To summarize, identifying the problems mentioned and suggesting suitable solutions is critical in developing a clear UAV channel measurement system.

In Chapter 4.1, the results of a measurement campaign for air-to-ground channels of UAV at 446MHz are presented due to the fact that refarming of UHF band will enable new opportunities for emergency case situations. Based on the measurement data, it is shown that altitude along with the environment is an important factor that needs to be considered. Due to the increase in the elevation, the channel condition gets better and the path loss exponent tends to decrease in general. Thus, in future studies, we will extend our results to multiple frequency ranges by also incorporating environmental effect in different locations and topographies.

In Chapter 5, presents the initial work for a better understanding of the characteristics of A2A wireless communications channels between UAVs by introducing a solid measurement–based modeling of large-scale LOS path loss components. The work provides insight into the hardnesses of developing a robust measurement setup for such a purpose, but more importantly, the extensive measurement campaign conducted introduces a large-scale A2A LOS path loss model for low altitude UAVs communicating in rural areas at 5.8 GHz. By performing measurements in both the anechoic chamber and outdoor environment with validation and statistical modeling purposes, it is shown that peculiar characteristics of the drones and A2A channels result in a PLE less than that of the free space path loss. The investigated channel sounding approach is shown to be worth being progressed since it has provided substantial channel knowledge despite being relatively very low-cost when compared to other sounding approaches. The proposed channel sounder provides a baseline for further analyses which is the future work, i.e., estimation of channel impulse response and higher-order channel statistics (e.g., excess delay spread, Doppler spectrum) for wider bands. Moreover, NLOS scenarios will be set up also to model shadowing and other fading characteristics.

The introduced measurement framework can also be used to optimize UAV flight duration, frequency domain estimation, and wireless coverage analysis. Further, this system can be exploited to understand the impact of drone body movement and drone body shift on wireless signal reception. Finally, measurement procedures can be developed to estimate the propagation environment in which drones are rapidly moving e.g., cases that require fast channel characterization.

REFERENCES

[1] **Shakhatreh, H.**, **Sawalmeh, A.H.**, **Al-Fuqaha, A.**, **Dou, Z.**, **Almaita, E.**, **Khalil, I.**, **Othman, N.S.**, **Khreishah, A. and Guizani, M.** (2019). Unmanned Aerial Vehicles (UAVs): A Survey on Civil Applications and Key Research Challenges, *IEEE Access*, *7*, 48572–48634.

[2] **Khuwaja, A.A.**, **Chen, Y.**, **Zhao, N.**, **Alouini, M.S. and Dobbins, P.** (2018). A survey of channel modeling for UAV communications, *IEEE Communications Surveys & Tutorials*, *20*(4), 2804–2821.

[3] **Willink, T.J.**, **Squires, C.C.**, **Colman, G.W.K. and Muccio, M.T.** (2016). Measurement and Characterization of Low-Altitude Air-to-Ground MIMO Channels, *IEEE Trans. Veh. Technol.*, *65*(4), 2637–2648.

[4] **Greenberg, E. and Levy, P.** (2017). Channel characteristics of UAV to ground links over multipath urban environments, *IEEE International Conference on Microwaves, Antennas, Communications and Electronic Systems*, pp.1–4.

[5] **Tu, K.**, **Rodríguez-Piñeiro, J.**, **Yin, X. and Tian, L.** (2019). Low Altitude Air-to-Ground Channel Modelling Based on Measurements in a Suburban Environment, *2019 11th International Conference on Wireless Communications and Signal Processing (WCSP)*, pp.1–6.

[6] **Athanasiadou, G.E. and Tsoulos, G.V.** (2019). Path Loss characteristics for UAV-to-Ground Wireless Channels, *2019 13th European Conference on Antennas and Propagation (EuCAP)*, pp.1–4.

[7] **Fessler, J.A. and Hero, A.O.** (1994). Space-alternating generalized expectation-maximization algorithm, *IEEE Trans. Signal Process.*, *42*(10), 2664–2677.

[8] **Mozaffari, M.**, **Saad, W.**, **Bennis, M. and Debbah, M.** (2015). Drone small cells in the clouds: Design, deployment and performance analysis, *2015 IEEE Global Communications Conference (GLOBECOM)*, IEEE, pp.1–6.

[9] **Tu, H.D. and Shimamoto, S.** (2009). A proposal of wide-band air-to-ground communication at airports employing 5-GHz band, *2009 IEEE Wireless Communications and Networking Conference*, IEEE, pp.1–6.

[10] **Al-Hourani, A. and Gomez, K.** (2017). Modeling cellular-to-UAV path-loss for suburban environments, *IEEE Wireless Communications Letters*, *7*(1), 82–85.

[11] **Yanmaz, E.**, **Kuschnig, R. and Bettstetter, C.** (2011). Channel measurements over 802.11 a-based UAV-to-ground links, *2011 IEEE GLOBECOM Workshops (GC Wkshps)*, IEEE, pp.1280–1284.

[12] **Feng, Q.**, **McGeehan, J.**, **Tameh, E.K. and Nix, A.R.** (2006). Path loss models for air-to-ground radio channels in urban environments, *2006 IEEE 63rd vehicular technology conference*, volume 6, IEEE, pp.2901–2905.

[13] **Feng, Q.**, **Tameh, E.K.**, **Nix, A.R. and McGeehan, J.** (2006). WLCp2-06: Modelling the likelihood of line-of-sight for air-to-ground radio propagation in urban environments, *IEEE Globecom 2006*, IEEE, pp.1–5.

[14] **Bor-Yaliniz, I.**, **Szyszkowicz, S.S. and Yanikomeroglu, H.** (2017). Environment-aware drone-base-station placements in modern metropolitans, *IEEE Wireless Communications Letters*, *7*(3), 372–375.

[15] **Weiner, M.** (1986). Use of the longley-rice and johnson-gierhart tropospheric radio propagation programs: 0.02-20 GHz, *IEEE Journal on Selected Areas in Communications*, *4*(2), 297–307.

[16] **Holis, J. and Pechac, P.** (2008). Elevation dependent shadowing model for mobile communications via high altitude platforms in built-up areas, *IEEE Transactions on Antennas and Propagation*, *56*(4), 1078–1084.

[17] **Zeng, L.**, **Cheng, X.**, **Wang, C.X. and Yin, X.** (2017). Second order statistics of non-isotropic UAV Ricean fading channels, *2017 IEEE 86th Vehicular Technology Conference (VTC-Fall)*, IEEE, pp.1–5.

[18] **Vinogradov, E.**, **Sallouha, H.**, **Bast, S.D.**, **Azari, M.M. and Pollin, S.** (2019). Tutorial on UAV: A Blue Sky View on Wireless Communication, *CoRR*, *abs/1901.02306*, `http://arxiv.org/abs/1901.02306`, `1901.02306`.

[19] **Simunek, M.**, **Fontán, F.P. and Pechac, P.** (2013). The UAV low elevation propagation channel in urban areas: Statistical analysis and time-series generator, *IEEE Transactions on Antennas and Propagation*, *61*(7), 3850–3858.

[20] **Al-Hourani, A.**, **Kandeepan, S. and Lardner, S.** (2014). Optimal LAP altitude for maximum coverage, *IEEE Wireless Communications Letters*, *3*(6), 569–572.

[21] **Al-Hourani, A.**, **Kandeepan, S. and Jamalipour, A.** (2014). Modeling air-to-ground path loss for low altitude platforms in urban environments, *2014 IEEE global communications conference*, IEEE, pp.2898–2904.

[22] **Liu, T.**, **Zhang, Z.**, **Jiang, H.**, **Qian, Y.**, **Liu, K.**, **Dang, J. and Wu, L.** (2019). Measurement-Based Characterization and Modeling for Low-Altitude UAV Air-to-Air Channels, *IEEE Access*, *7*, 98832–98840.

[23] **Ma, Z.**, **Ai, B.**, **He, R. and Zhong, Z.** (2019). A 3D Air-to-Air Wideband Non-Stationary Channel Model of UAV Communications, *IEEE Vehicular Technology Conference*, pp.1–5.

[24] **Ma, Z.**, **Ai, B.**, **He, R.**, **Wang, G.**, **Niu, Y. and Zhong, Z.** (2019). A Wideband Non-Stationary Air-to-Air Channel Model for UAV Communications, *IEEE Trans. Veh. Technol.*

[25] **Liu, T.**, **Zhang, Z.**, **Jiang, H.**, **Qian, Y.**, **Liu, K.**, **Dang, J. and Wu, L.** (2019). Measurement-Based Characterization and Modeling for Low-Altitude UAV Air-to-Air Channels, *IEEE Access*, *7*, 98832–98840.

[26] **Amorim, R.**, **Nguyen, H.**, **Mogensen, P.**, **Kovács, I.Z.**, **Wigard, J. and Sørensen, T.B.** (2017). Radio channel modeling for UAV communication over cellular networks, *IEEE Wireless Communications Letters*, *6*(4), 514–517.

[27] **Zhang, Y.**, **Wen, J.**, **Yang, G.**, **He, Z. and Luo, X.** (2018). Air-to-air path loss prediction based on machine learning methods in urban environments, *Wireless Communications and Mobile Computing*, *2018*.

[28] **Amorim, R.**, **Mogensen, P.**, **Sorensen, T.**, **Kovács, I.Z. and Wigard, J.** (2017). Pathloss measurements and modeling for UAVs connected to cellular networks, *2017 IEEE 85th Vehicular Technology Conference (VTC Spring)*, IEEE, pp.1–6.

[29] **Erem, O.** (2019). İstanbul’da 5,8 büyüklüğünde deprem, *BBC*, `https://www.bbc.com/turkce/live/haberler-turkiye-49836320`.

[30] **Report, E.**, ECC Report: Harmonised conditions and spectrum bands for the implementation of future European Broadband Public Protection and Disaster Relief (BB-PPDR) systems, Available: `https://www.ecodocdb.dk/download/bf3fb2b0-9509/ECCREP218.PDF`, Accessed: Oct. 29, 2019.

[31] **del Rey Carrión, D.**, **Juan-Llácer, L. and Rodríguez, J.V.** (2019). Radio Planning Considerations in TETRA to LTE Migration for PPDR Systems: A Radioelectric Coverage Case Study, *Applied Sciences*, *9*(2), 250.

[32] **Sanchoyerto, A.**, **Solozabal, R.**, **Blanco, B. and Liberal, F.** (2019). Analysis of the Impact of the Evolution Toward 5G Architectures on Mission Critical Push-to-Talk Services, *IEEE Access*, *7*, 115052–115061.

[33] **Lodro, M.**, **Gradoni, G.**, **Vukovic, A.**, **Thomas, D. and Greedy, S.** (2020). Time-Domain Wireless Channel Sounding Using Software Defined Radio, *2020 3rd International Conference on Computing, Mathematics and Engineering Technologies (iCoMET)*, pp.1–5.

[34] **Walrand, J. and Varaiya, P.**, (2000). CHAPTER 7 - Wireless Networks, **J. Walrand and P. Varaiya**, editors, High-Performance Communication Networks (Second Edition), Morgan Kaufmann, San Francisco, second edition edition, pp.305–361, `https://www.sciencedirect.com/science/article/pii/B9780080508030500125`.

[35] **Rappaport, T.S.** *et al.* (2015). *Wireless Communications: Principles and Practice*, volume 2, Prentice Hall.

[36] **Alonso, D.**, **Gavilán, J. and Dostert, K.** (2016). Software Defined Channel Sounder for Power Line Communications, **Technical Report**, Karlsruher Institut für Technologie (KIT).

[37] **Instruments, N.**, (2019), USRP E312, `https://www.ettus.com/wp-content/uploads/2019/01/USRP_E312_Datasheet.pdf`, original document from National Instruments.

[38] **Instruments, N.**, (2019), USRP B210, `https://www.ettus.com/wp-content/uploads/2019/01/b200-b210_spec_sheet.pdf`, original document from National Instruments.

[39] Analog Devices Transmit LO Leakage (LOL)—An Issue of Zero-IF That Isn't Making People Laugh Out Loud, `https://tinyurl.com/uvbjkcj`, accessed: 2019-12-26.

[40] **Moseley, N.A. and Slump, C.H.** (2006). A low-complexity feed-forward I/Q imbalance compensation algorithm, *17th Annual Workshop on Circuits*, pp.158–164.

[41] S.W. Ellingson Correcting I-Q Imbalance in Direct Conversion Receivers, `https://www.faculty.ece.vt.edu/swe/argus/iqbal.pdf`, accessed: 2019-12-31.

[42] **Anttila, L.**, **Valkama, M. and Renfors, M.** (2007). Blind compensation of frequency-selective I/Q imbalances in quadrature radio receivers: Circularity-based approach, *2007 IEEE International Conference on Acoustics, Speech and Signal Processing-ICASSP'07*, volume 3, IEEE, pp.III–245.

[43] **Yan, C.**, **Fu, L.**, **Zhang, J. and Wang, J.** (2019). A comprehensive survey on UAV communication channel modeling, *IEEE Access*, *7*, 107769–107792.

[44] **Yılmaz, A. and Toker, C.** (2022). Air-to-Air Channel Model for UAV Communications, *2022 30th Signal Processing and Communications Applications Conference (SIU)*, pp.1–4.

[45] **Allen, J.B. and Rabiner, L.R.** (1977). A unified approach to short-time Fourier analysis and synthesis, *Proceedings of the IEEE*, *65*(11), 1558–1564.

[46] **Kaplan, B.**, **Kahraman, İ.**, **Görçin, A.**, **Çırpan, H.A. and Ekti, A.R.** (2020). Measurement based FHSS–type Drone Controller Detection at 2.4 GHz: An STFT Approach, *2020 IEEE 91st Vehicular Technology Conference (VTC2020-Spring)*, IEEE, pp.1–6.

[47] **Allred, J.**, **Hasan, A.B.**, **Panichsakul, S.**, **Pisano, W.**, **Gray, P.**, **Huang, J.**, **Han, R.**, **Lawrence, D. and Mohseni, K.** (2007). Sensorflock: an airborne wireless sensor network of micro-air vehicles, *Proceedings of the 5th international conference on Embedded networked sensor systems*, pp.117–129.

CURRICULUM VITAE

Name Surname : Burak EDE

EDUCATION :

- **B.Sc.** : 2017, Istanbul Technical University, Faculty of Electrical and Electronics, Department of Electronics and Communication Engineering

PROFESSIONAL EXPERIENCE AND REWARDS:

- **07.2018–12.2018 :** STARTECH Electronics and Computer Systems. Industry Trade. LLC.
- **02-2019–08.2019 :** YALTES Electronics and Information Systems Production and Trade Inc.
- **08-2019–** Researcher at The Scientific and Technological Research Council of Turkey (Informatics and Information Security Research Center)

PUBLICATIONS, PRESENTATIONS AND PATENTS ON THE THESIS:

- **Ede, B.**, Ekti, A.R., Yarkan, S., Baykas, T., Cirpan, H.A., Gorcin, A. (2020, May). “Measurement Based Statistical Channel Characterization of Air-to-Ground Path Loss Model at 446 MHz for Narrow-Band Signals in Low Altitude UAVs”, *IEEE Vehicular Technology Conference (VTC).*

- **Ede, B.**, Kaplan, B., Kahraman, İ., Keşir, S., Yarkan, S., Baykas, T., Ekti, A.R., Gorcin, A, Cirpan, H.A. (2021, October). “Measurement-Based Large Scale Statistical Modeling of Air-to-Air Wireless UAV Channels via Novel Time-Frequency Analysis,” *IEEE Wireless Communications Letters*, doi: 10.1109/LWC.2021.3122281.

B. EDE

MEASUREMENT BASED AIR TO AIR AND AIR TO
GROUND DRONE COMMUNICATION CHANNEL MODELING

2023